



UNESCO Chair on  
Coastal Geo-Hazard Analysis

Research Institute for Earth Sciences  
Geological Survey of Iran



Chair



UNESCO Chair on  
Coastal Geo-Hazard Analysis

Research Institute for Earth Sciences  
Geological Survey of Iran



Chair

## Abstract:

The Astara Fault System (AFS) is located in the northwest Alborz, east of Talesh Mountain (TM) and west of South Caspian Basin (SCB). The AFS is heavily involved in seismotectonic of Talesh region and to which subsidence of SCB is attributed. There is little information available concerning the AFS previous seismic activities and its properties. In order to elucidate the seismic behavior and activities of the AFS, we conducted a research study on paleoseismology of the fault. Based on paleoseismic evidence, two scenarios could be taken into consideration, one of which has 3 and another has 4 seismic events with magnitudes  $M_w$  in the range of 6.7 to 7.2. Evidence of these seismic events are within sedimentary succession as they have occurred during the past 3ka (this age is determined based on the deposition rate of the region). Six carbon samples were taken for  $^{14}C$  age determination test, the results of which clearly demonstrated that the EvIV (scenario A) and EvIII (scenario B) had occurred before 27444 cal BP while other events occurred in the time period between 27444 cal BP and 3ka ago. If we consider occurrence of three or four seismic events (based on the two scenarios) to be between 27444 cal BP and 3ka ago, the average recurrence interval is  $7119 \pm 1017$  but the evidence of these events have been removed. If we assume the EvI to be the earliest event (at both scenarios), the minimum elapsed time is therefore, 3ka. However, if we assume that the last event occurred at a time before  $10995 \pm 50$  ago (based on C14 age determination test), EvII at scenario A, the maximum elapsed time is therefore,  $10995 \pm 50$ .



## Paleoseismological Analysis along the Astara Fault System (Talesh Mountains, North Iran)

UCCGHA 014

ISBN: 978-622-5858-52-7

2023



9 786225 858527

2023

**Paleoseismological Analysis  
along the Astara Fault System  
(Talesh Mountains, North Iran)**



- سرشناسه : برزگری، امیر، ۱۳۴۵-  
-Barzegari, Amir, 1986
- عنوان و نام پدیدآور : Paleoseismological Analysis along the Astara Fault System (Talesh Mountains, North Iran)[Book]/authors Amir Barzegari...[et al.]; employer Research Institute for Earth Sciences; advisor Islamic Azad University- North Tehran Branch; with cooperation UNESCO Chair on Coastal Geo-Hazard Analysis; supervisors Manouchehr Ghorashi, Hamid Nazari; summarized Manouchehr Ghorashi.
- مشخصات نشر : تهران: نشر خزه، ۱۴۰۲ = ۲۰۲۳ م.  
مشخصات ظاهری : ۷۸ص.: مصور؛ ۱۴ × ۲۱ سم.  
شابک : 978-622-5858-52-7
- وضعیت فهرست نویسی : فیبا  
یادداشت : زبان: انگلیسی.  
یادداشت : Authors Amir Barzegari, Michel Fontugne, Mohammad Ali Shokri, Mohsen PurKermani
- یادداشت : عنوان به فارسی: تحلیل پارینه لرزه‌شناسی در امتداد سامانه گسلی آستارا (کوه های تالش، شمال‌ایران).  
گسله‌ها -- ایران -- آستارا
- موضوع : Faults (Geology) -- Iran -- Astara  
موضوع : دیرینه لرزه شناسی  
موضوع : Paleoseismology  
شناسه افزوده : قرشی، منوچهر، ۱۳۳۰-، ناظر  
شناسه افزوده : Ghorashi, Manouchehr  
شناسه افزوده : نظری، حمید، ۱۳۴۶-، ناظر  
شناسه افزوده : Nazari, Hamid, 1967-  
شناسه افزوده : یونسکو. کرسی مخاطرات زمین شناختی ساحلی  
شناسه افزوده : UNESCO Chair on Coastal Geo-Hazard Analysis  
شناسه افزوده : پژوهشکده علوم زمین  
شناسه افزوده : Research Institute for Earth sciences
- رده بندی کنگره : ۲/QE۵۳۷  
رده بندی دیویی : ۲۲۰۹۵۵۳۳۴۶/۵۵۱  
شماره کتابشناسی ملی : ۹۳۶۳۹۸۶

# **Paleoseismological Analysis along the Astara Fault System (Talesh Mountains, North Iran)**

**Author: Amir Barzegari**





UNESCO Chair on  
Coastal Geo-Hazard Analysis

Research Institute for Earth Sciences  
Geological Survey of Iran



## اطلاعات گزارش

**عنوان:** تحلیل پارینه لرزه‌شناسی در امتداد سامانه گسلی آستارا (کوه‌های تالش، شمال ایران)

**مجری:** پژوهشکده علوم زمین

**مشاور:** دانشگاه آزاد اسلامی - واحد تهران شمال

**زبان مرجع:** انگلیسی

**خروجی:** نقشه، مقاله، داده‌های الکترونیکی

**ناظر علمی:** منوچهر قرشی، حمید نظری

**نویسندگان:** امیر برزگری، میشل فونتوگنه، محمدعلی شکری، محسن پورکرمانی

**رئیس کرسی یونسکو در مخاطرات زمین شناختی ساحلی:** حمید نظری

**مسئول شورای اجرایی:** راضیه لک

**خلاصه‌نویسی:** منوچهر قرشی

**خلاصه شده از:** طرح مخاطرات زمین شناسی دریایی حوضه جنوب کاسپین

**ناشر:** نشر خزه

**با همکاری کرسی یونسکو در مخاطرات زمین شناختی ساحلی**

**چاپ اول:** ۱۴۰۲

**شمارگان:** ۵۰ نسخه

**صفحات:** ۷۸

**شابک:** ۹۷۸-۶۲۲-۵۸۵۸-۵۲-۷

[khazepub@gmail.com](mailto:khazepub@gmail.com)



UNESCO Chair on  
Coastal Geo-Hazard Analysis  
Research Institute for Earth Sciences  
Geological Survey of Iran



## Report Information

---

**Title:** Paleoseismological Analysis along the Astara Fault System (Talesh Mountains, North Iran)

**Employer:** Research Institute for Earth Sciences

**Advisor:** Islamic Azad University- North Tehran Branch

**Original language:** English

**Output:** Map, Paper, Digital meta data

**Supervisors:** Manouchehr Ghorashi, Hamid Nazari

**Authors:** Amir Barzegari, Michel Fontugne, Mohammad Ali Shokri, Mohsen PurKermani

**Chairholder in the UNESCO Chair on Coastal Geo-Hazard Analysis:**  
Hamid Nazari

**Head of the Executive Council:** Razyeh Lak

**Summarized:** Manouchehr Ghorashi

**Summarized after:** Geohazard South Caspian Carpet (GSCC)

**Publisher:** Khazeh Publication

with cooperation UNESCO Chair on Coastal Geo-Hazard Analysis

**First Edition:** 2023

**Edition number:** 50

**Page:** 78

**Shabak:** 978-622-5858-52-7

[khazepub@gmail.com](mailto:khazepub@gmail.com)



## Scientific Council

<b>Name</b>	<b>Affiliation</b>
Ara Avagyan	IGS: Institute Geological Sciences
Rick J Bailey	IOC-UNESCO Indian Ocean Tsunami Warning and Mitigation System/ UNESCO
Aram Fathian Baneh	University of Calgary
Wenjiao Xiao	Chinese Academy of Sciences
Philippe Agard	University of Sorbonne
Eric Barrier	University of Sorbonne
Justin Ahanhanzo	Intergovernmental Oceanographic Commission of UNESCO (IOC- UNESCO)
Alice Aurelie	UNESCO Water Sciences Division
Klaus Reicherter	Aachen University
Judith Thomalsky	German Archaeological Institute Tehran Branch
Martin Hanz	German under water archaeology association
Hamid Alizadeh Lahijani	Iranian National Institute for Oceanography and Atmospheric Science
Yahya Djamour	Shahid Beheshti University (SBU)
Hassan Fazeli Nashli	University of Tehran
Razyeh Lak	Research Institute for Earth Sciences
Mohammad Mokhtari	International Institute of Earthquake Engineering and Seismology
Hamid Nazari	Research Institute for Earth Sciences

Jafar Omrani	Geological Survey of Iran
Mohammad Tatar	International Institute of Earthquake Engineering and Seismology
Morteza Talebian	Research Institute for Earth Sciences
Mehdi Zare	International Institute of Earthquake Engineering and Seismology
Stefano Salvi	National Institute of Geophysics and Volcanology (INGV)
Ryo Anma	Tokushima University
John Lambert	Deltares, UNESCO
Issa El-Hussain	Sultan Qaboos University
Egor Krasinskiy	Underwater research center Russian Geographical Society
Richard Walker	University of Oxford
Audemard Franck A.	Department of Geology, Central University of Venezuela
Wenjiao Xiao	Chinese Academy of Sciences
Jean-François Ritz	University of Montpellier
Ekkehard Holzbecher	German University of Technology in Oman
Yeong Bae Seong	Korea University

### **Executive Committee**

<b>Name</b>	<b>Affiliation</b>
Dr. Razyeh Lak	Head of RIES and Executive Manager
Mahmoudreza Majidifard	Research Institute for Earth Sciences
Manouchehr Ghorashi	Research Institute for Earth Sciences
Alireza Vaezi	Research Institute for Earth Sciences
Arash Amini	Golestan University

Mohammad Tatar	International Institute of Earthquake Engineering and Seismology
Mohammad reza Ghasemi	Research Institute for Earth Sciences
Jafar Hassanpour	University of Tehran
Ataollah Dadashpour	Geological Survey of Iran, Sari branch
Ahmadreza Rabani	University of Science and Technology of Mazandaran
Ahmad Rashidi	International Institute of Earthquake Engineering and Seismology
Masoud Sadri Nasab	University of Tehran
Hasan Fazelinashli	University of Tehran
Abdolazaim Ghanghormeh	Golestan University
Ataollah Kaviani	Environmental Protection Organization of Mazandaran Province
Seyed Mohsen Mortazavi	Hormozgan University
Nasir Ahmadi	Environmental Protection Organization of Mazandaran Province
Hasan Nasrollah Zadeh Saravi	Caspian Sea Ecological Research Center
Mojtaba Yamani	University of Tehran
Ahmed Hadidi	German University of Technology in Oman (GUTECH)
Alireza Amrikazemi	Scientific Coordinator, Qeshm Island UNESCO Global Geopark
Mahdi Rahmanian	Shargh Daily newspaper
Mohammad Salamati	Respina Company
Mohammadreza Kazemzadeh	Superme Audit Gourt

## **Secretariat**

<b>Name</b>	<b>Affiliation</b>
Elnaz Aghaali	Research Institute for Earth Sciences
Hamoon Memarian	Research Institute for Earth Sciences
Hourieh AliBeygi	Research Institute for Earth Sciences
Shirin Zarei	Research Institute for Earth Sciences
Keivan Ajdari	Research Institute for Earth Sciences
Sedigheh Ghanipour	Research Institute for Earth Sciences
Shirin Safavi	Research Institute for Earth Sciences
Leila Shirazi	Research Institute for Earth Sciences
Aazam Takhtchin	Research Institute for Earth Sciences
Hanieh Bakhshaei	Geological Survey of Iran
Reza Behbahani	Geological Survey of Iran
Javad Darvishi khatooni	Geological Survey of Iran
Mohammadreza Ensani	Geological Survey of Iran
Marziyeh Estrabi Ashtiyani	Geological Survey of Iran
Gholamreza Hoseinyar	Geological Survey of Iran
Mojtaba Kavianpour Sangno	Geological Survey of Iran
Mehrnoosh Pour Saeid	Graphic Designer

## Contents

ABSTRACT.....	1
1- INTRODUCTION .....	2
2- TECTONIC SETTING.....	4
3- MORPHOTECTONICS .....	9
4- KINEMATICS OF ASF .....	12
5- PALAEOSEISMOLOGY.....	13
5-1- <i>SITE SELECTION</i> .....	13
5-2- <i>STRATIGRAPHY AND AGE OF UNITS</i> .....	15
5-3- <i>SEISMIC EVENTS</i> .....	26
5-3-1- <i>Scenario A</i> .....	34
5-3-2- <i>Scenario B</i> .....	47
6- SEISMIC BEHAVIOURS.....	50
6-1- <i>MAGNITUDE OF PALEOEARTHQUAKES</i> .....	50
6-2- <i>RECURRENCE INTERVALS OF EARTHQUAKE</i> .....	52
6-3- <i>ELAPSED TIME</i> .....	53
7- CONCLUSIONS .....	55
References.....	57

## Table of Figures

Figure 1: Simplified tectonic map of Iran and surrounding area (modified after Venant et al., 2004) on which is superimposed SRTM data with a position resolution of 90m. Ash: Ashkabad fault, AFS: Astara Fault System, Deh: Dehshir fault, KB: Kuh Banan fault, MRF: Main Recent Fault, MZT: Main Zagros Thrust, Nay: Nayband fault. The white rectangle corresponds to the Figure2.....	3
Figure 2: A) Seismotectonic map of NW Iran, See fig.1 for location. The red line with triangles and the red line with arrows show the reverse and shear faults, respectively. The black and green focal mechanisms are those reported by Harvard CMT and Jackson et al., 2002, respectively. The black elliptical shapes show the meizoseismal area of earthquakes (modified after Nazari et al., 2013). White rectangle shows the location of map B. B) Seismotectonic map of TM. Descriptions of red lines are same as fig A. The light pink, magenta, walnut, orange and deep violent circles show Mw, Ms, mb, Ml and Mn. The green star shows the studied area in Lisar River (modified after Kaveh et al., 2013). .....	8
Figure 3: Map of the morphotectonic features observed in Gillan province from DEM30 m ( <a href="http://dds.cr.usgs.gov/srtm/version2_1/SRTM30//srtm30">http://dds.cr.usgs.gov/srtm/version2_1/SRTM30//srtm30</a> ): yellow lines, blue lines and red lines show crest lines, drainages and fault branches of AFS (Kaveh et al.,2013), respectively. Rectangle enclosed areas are shown in the following figures.....	12
Figure 4: a) The Google Earth image of fault scarp, see fig.3 for locations. The black lines represent the GPR profiles at the fig. b and c. b and c show the GPR profile at A - A' and B-B'	

lines, respectively. Orange arrows and green lines at b and c represent the base of pavement and vertical anomaly, respectively. The GPR results are taken from Mohammadi Vijeh., (2013)..... 15

Figure 5: a) The Google Earth image of fault scarp, see fig.3 for locations. The black lines represent the GPR profiles at the fig. b and c. b and c show the GPR profile at A - A' and B-B' profiles, respectively. Orange arrows and green lines at b and c represent the base of pavement and vertical anomaly, respectively. The GPR results are taken from Mohammadi Vijeh., (2013)..... 17

Figure 6: a) Google earth view of the scarp and offset of the river, see fig.3 for location. Red triangles denote the thrust faults segments (Kaveh et al, 2013). Dash green line represents the probable segment of AFS. Orange star denotes the abrupt change in elevation at fig. c, this scarp has N308 trend. The light blue triangles and A-A' represent the right lateral offset of the river ( $32\pm 2$  m). white rectangle denotes the fig. b. b) Closer view of right lateral offset of the river (light blue arrows) on the Google earth image and scarp (orange star). c) The field photo at the star location in fig. 6a and 6b..... 18

Figure 7: a) DEM 30 m view at 317868/4178924 UTM coordinate, see fig.3 for location. Light green triangles, black line and orange star denote the scarp trend, longitudinal profile and location of the abrupt change in elevation, respectively. b) Longitudinal profile at A-A' line (see image a for location). c) The field photo. The light green triangles represent the fault scarp. .... 22

Figure 8: a) Diagram depicting The magnetic anomaly at shutter ridge. The black line shows the ASF fault. b) The magnetic anomaly Diagram on a Google earth image. The black and white lines along with orange dash line denote the

scan line, ASF and shutter ridge, respectively. Q (t) and Pe (v.t) are quaternary alluvium and andesitic tuff, respectively (Asadi, 2013).c) the field photo of the shutter ridge. .... 23

Figure 9: a) Google earth view at scarp and offset of river. The yellow, red, blue triangles and dash green line denote the strike slip, thrust, right lateral offset of river and probable segments of AFS, respectively. The orange and white rectangles represent fig. b and c, respectively. See fig.3 for locations. b) The field photo of scarp, the red triangles denote the scarp and abrupt change of elevation. c) The closer view at the right lateral offset. red triangles, green dash line, blue line and A-A' represent the thrust fault, probable segments of AFS, river and river offset ( $33\pm 2m$ ). d) The field photo of right lateral displacement in the river. .... 24

Figure 10: see fig. 3 for location. In this field photo two points are shown, one of them is dextral offset at river that is represented with blue arrows and another is shutter ridge feature that is denoted with red arrows. The red dash line with sense motion shows the probable of ASF segments. .... 25

Figure 11: Calculation of trigonometric relationships.  $V_f$ =the vertical offset measured on the riverbank,  $H_f$ = the horizontal displacement stems from the  $V_f$  and different rake values,  $V$  and  $H$  respectively representing the throw and heave of fault,  $\rho$ =rake,  $\delta$ =dip of fault,  $AC$ = resultant displacement component in two and three dimensions. .... 27

Figure 12: a) The topographic map that stems from Dem 10 m at the dextral displacement of river. The green, magenta, dark blue and dash red lines show the profile survey at fig. c, river and probable fault segment, respectively. The vertical interval of each counter is 1 meter. b) The 3D modeling of the studied area. c) The estimation of rake value based on fig. 10. .... 29

Figure 13: a) The topographic map that stem from Dem 10 m at the dextral displacement of the river. The green, magenta,

dark blue and dash red lines show the profile survey at fig. c, river and probable fault segment, respectively. The vertical interval of each counter is 1 meter. b) The 3D modeling of the studied area. c) The estimation of rake value based on fig.10.

..... 31

Figure 14: a) Field photo of the south bank. b) Corresponding cartoon drawing of the bank. Yellow, brown and grey parts in drawing sketch are indication of the clay part and the clastic layer, respectively. .... 33

Figure 15: a) A Google Earth image of Lisar river in which the AFS branch is shown, see fig. 3 for location. Rectangles b and c denote on d and f figures, respectively. d) field picture of right lateral displacement that is represented with rectangle b in image a. solid blue line shows recent river flow and displacement amount is shown with orange color. e) 3D model of rectangle b, dash black line is representative of the river and red line with triangle is an indication of AFS branch (reverse fault with right lateral component). f) field picture of rectangle c in image a, blue arrow shows right lateral displacement of river flow and green arrow is showing the sand mine. g) Diagram depicting magnetic anomaly of Lisar river which is showing 4 anomalies, anomaly number 2 conforms with AFS branch which is drawn by Kaveh et al, 2013 (Asadi, 2013)..... 36

Figure 16: a) photomosaic of Lisar River wall (see Fig. 2 for location). b) Respective log, with labels marking the stratigraphic units..... 39

Figure 17: Schematic views of Lisar riverbank log based on the scenario A from the present day (Step1) back to before the oldest event occurrence (Step 30). .... 45

Figure 18: Schematic views of Lisar riverbank log based on the scenario B..... 49

Figure 19: Probability distribution based on results of six <sup>14</sup>C dating samples tests..... 52

Figure 20: The graph shows the horizontal offsets projected on earth Hf versus the median age (Cal BP)..... 54

## **ABSTRACT**

The Astara Fault System (AFS) is located in the northwest Alborz, east of Talesh Mountain (TM) and west of South Caspian Basin (SCB). The AFS is heavily involved in seismotectonic of Talesh region and to which subsidence of SCB is attributed. There is little information available concerning the AFS previous seismic activities and its properties. In order to elucidate the seismic behavior and activities of the AFS, we conducted a research study on paleoseismology of the fault. Based on paleoseismic evidence, two scenarios could be taken into consideration, one of which has 3 and another has 4 seismic events with magnitudes  $M_w$  in the range of 6.7 to 7.2. Evidence of these seismic events are within sedimentary succession as they have occurred during the past 3ka (this age is determined based on the deposition rate of the region). Six carbon samples were taken for  $^{14}\text{C}$  age determination test, the results of which clearly demonstrated that the EvIV (scenario A) and EvIII (scenario B) had occurred before 27444 cal BP while other events occurred in the time period between 27444 cal BP and 3ka ago. If we consider occurrence of three or four seismic events (based on the two scenarios) to be between 27444 cal BP and 3ka ago, the average recurrence interval is  $7119 \pm 1017$  but the evidence of these events have been removed. If we assume the EvI to be the earliest event (at both scenarios), the minimum elapsed time is therefore, 3ka. However, if we assume that the last event occurred at a time before  $10995 \pm 50$

ago (based on C14 age determination test), EvII at scenario A, the maximum elapsed time is therefore,  $10995 \pm 50$ .

## **1- INTRODUCTION**

The Astara Fault System (AFS) has a north to south trend, located in the northwest Central Alborz, east of Talesh Mountain (TM) and west of South Caspian Sea (e.g. Zanjani et al., 2013, Kaveh et al., 2013, Khodabanehd et al., 1997, Jackson et al., 2002, Allen et al., 2003, Hessami et al., 2003, Rahimzadeh et al., 1987) (Figure 1 & Figure 2). The trend of AFS coincides with the F-270 magnetic lineament (Yousefi, & Friedberg, 1978) and metamorphic basement rock is exposed at the west of AFS. These are two reasons why this fault is regarded as one of the basement rock faults in Iran. The AFS has contributed heavily to seismotectonic of Talesh region and the subsidence to the west of the SCB under TM is induced by this fault system (Jackson et al., 2002).

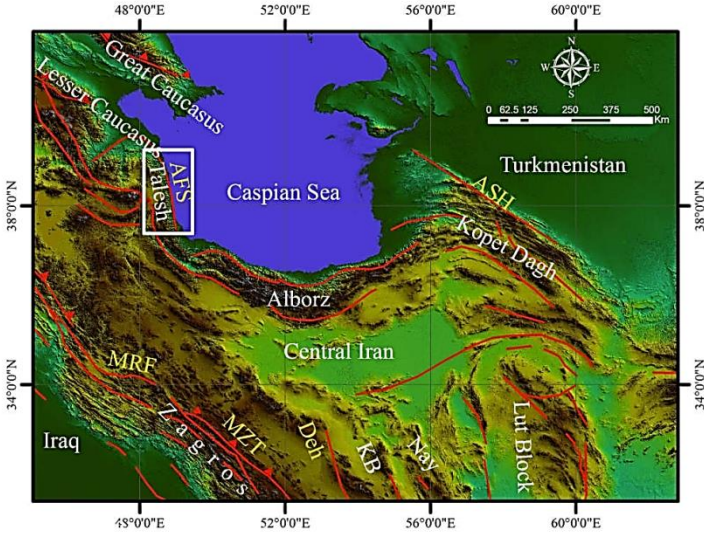


Figure 1: Simplified tectonic map of Iran and surrounding area (modified after Venant et al., 2004) on which is superimposed SRTM data with a position resolution of 90m. Ash: Ashkabad fault, AFS: Astara Fault System, Deh: Dehshir fault, KB: Kuh Banan fault, MRF: Main Recent Fault, MZT: Main Zagros Thrust, Nay: Nayband fault. The white rectangle corresponds to the Figure2.

The AFS could be the source of moderate to large-magnitude instrumental earthquakes on 16-4- 1913 (Magnitude=5.1), 11-7-1970 (Magnitude  $m_b=5.2$ ), 4-11-1978 (Magnitude  $M_s=6.0$ ) (Berberian. 1983). Historical seismic data regarding AFS activities are not clear. However, AFS is assumed to be the cause of historical earthquakes of Rasht city in 1709AD and 1713AD

(Ambraseys and Melville, 1982; Berberian & Yeats 1999, 2001; Nazari and Shahidi, 2011).

No general consensus has yet reached among researchers on AFS mechanism and dip directions. Berberian (1983) believed that this fault is Reverse and is dipping toward west, whereas in the 1: 100,000 scaled geological map of Astara region, it is represented as a Strike slip fault with right lateral component (Khodabanedh et al.,1997). Kaveh et al., (2013) subscribe to the view that AFS has two types of fault mechanisms with sections towards the Caspian Sea have strike slip mechanism while sections adjacent to the TM have thrust mechanism with a right lateral strike slip component (Figure 2 b) and generally, under either of these mechanisms the fault has westward dip direction (Figure 2 b) (Jakson et al., 2002). AFS passes the Gilan province (with a population of 2,453,469) and its seismic activities affect the region (Figure 2 a and b). Since AFS is in the vicinity of the SCB and Talesh Mountain, it is assumed that the seismic activities of AFS could be the cause of land slide at TM and tsunami waves in SCB.

## **2- TECTONIC SETTING**

The present structure of the studied area and its seismic behavior are affected by the Arabia-Eurasia continental collision and clockwise rotation of the SCB (Zanjani et al., 2013. Jackson et al., 2002); the recent GPS data analysis results concur with this view (Djamour et al, 2010). In contrast to the TM, the SCB is

an aseismic block and one of the hypotheses made concerning it, is that the SCB is the back arc basin residual of the Tethyan Mesozoic arc (e.g. Berberian, 1983; Brunet et al, 2003; Kaz'min & Verzhbitskii, 2011, Zanjani et al, 2013). The basement of SCB has uncommon properties of a thick oceanic crust or continental crusts in which seismic waves propagate at high velocities. This basement is covered with 20 km thick sedimentary sequence (Brunet et al., 2003, Knapp et al., 2004, Kaz'min & Verzhbitskii 2011, Neprochnov, 1968, Darvishzade, 1992, Mangino and Priestly, 1998). Jackson et al., (2002) estimated the present motions of SCB relative to Iran and Eurasia. They showed that the SCB is moving 13-17 mm/yr and 8-10 mm/yr, SW relative to Iran and NW relative to Eurasia, respectively. The SCB is surrounded by the active folds and seismic belts of the TM to the west, Alborz to the south and Kopeh Dag to the east all of which subject SCB to their thrust action (Figure 1). At its north side, SCB is limited by Apsheron–Balkhan sill and in contrast with other sides, the earthquakes in this area occur at the depth of at least 80 km which indicates that the SCB is subducting beneath the Central Caspian (Jackson et al., 2002). Considering the rotation and motion of SCB it has been suggested that SCB is underthrusting beneath the TM in Iran and Azerbaijan (Jackson et al., 2002) albeit this is a controversial issue (Zanjani et al., 2013). The Talesh Mountain is located at the westward extension of Alborz Mountain with a width less than 50 km (Figure 1). The rocks that have formed the TM, are the same as Alborz

Mountain rocks and include thick Paleogene andesitic volcanoclastic sequences (Jackson et al., 2002). The interactions between Talesh and Alborz with SCB and the rotation of SCB have an impact on the structural shaping of the southern and northern faces of TM, respectively. Thus, the deformations at northern and southern parts are more drastic than the central part of TM (Zanjani et al., 2013). The TM is a bended fold and thrust belt with N-S direction but at north, where TM meets the Kura Basin the thrusts trend is inclined to E-W direction (Jackson et al., 2002; Allen et al., 2003). The earthquake mechanisms of TM are different from those of Alborz Mountain and they are clear indications of almost flat faults at depths of 15–26 km, which are deeper than the depths observed at Alborz Mountain and slip vectors are inclined towards the Caspian Sea. The centroid depths of these earthquakes represent thrusting of the crystalline basement of the Caspian westwards beneath the Talesh Mountains. Based on reconstruction of folding and thrusting, the shortening of NW part of TM is estimated to be about 25 Km, which is identical to shortening of SW part of the Alborz Mountain (Jackson et al., 2002). According to recent GPS data the TM is moving in the direction of the N – NW (Djamour et al., 2010). Zanjani et al., (2013) has showed the depth of seismicity along the Caspian coastline to vary from 20 to 47 Km but these depths at inland and west of AFS are in the range of 20-25 km. One of the active structures at southern and central parts are Masuleh and Boghrov faults whose dips are toward the NE (e.g. Davies et al.,

1972, Berberian & Yeats 1999, Zanjani et al., 2013). The Masuleh fault is thrusting the Paleozoic carbonate and clastic rock units over Eocene volcanic rock units and presence of right lateral offsets of drainages is an indication of the strike – slip mechanism. The Boghrov Dagh Fault includes several hanging wall and footwall strands and its length is more than 120 km (Davies et al., 1972, Berberian & Yeats.1999, Zanjani et al., 2013). Highly vegetative cover and erodible rock units have resulted in lack of sufficient evidence for the aspects of recent activities of the Boghrov Dagh Fault (Zanjani et al., 2013).

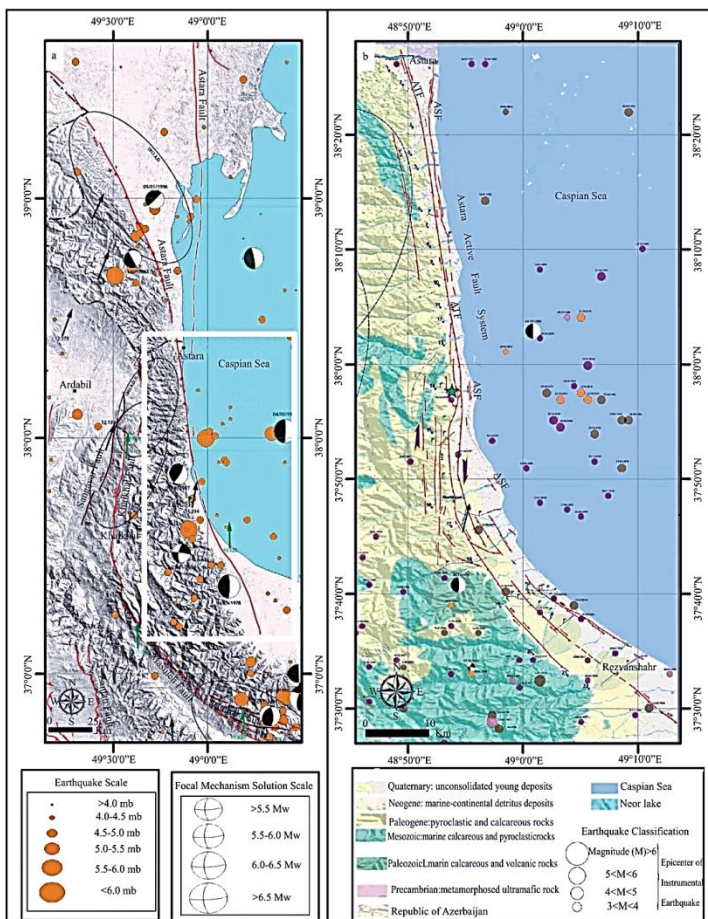


Figure 2: A) Seismotectonic map of NW Iran, See fig.1 for location. The red line with triangles and the red line with arrows show the reverse and shear faults, respectively. The black and green focal mechanisms are those reported by Harvard CMT and Jackson et al., 2002, respectively. The black elliptical shapes show the meizoseismal area of earthquakes (modified after Nazari et al., 2013). White

rectangle shows the location of map B. B) Seismotectonic map of TM. Descriptions of red lines are same as fig A. The light pink, magenta, walnut, orange and deep violet circles show Mw, Ms, mb, Ml and Mn. The green star shows the studied area in Lisar River (modified after Kaveh et al., 2013).

### **3- MORPHOTECTONICS**

Owing to the fact that the region surrounding the AFS is heavily populated and the forest coverage is generally dense, there is a huge amount of uncertainty concerning the AFS and its properties which hinders all attempts for execution of morphotectonics studies. The first step to the analysis carried out in this section is based on field observation and digital elevation models (DEM); then, geophysical approaches (such as Magnetic method, Electrical resistivity survey (or RS) and Ground Penetration Radar (or GPR)) are utilized to corroborate the observation made in the previous step (Figure 4, Figure 5 & Figure 8) (McCalpin, 2009; Asadi, 2013). Figure 3 shows the morphotectonics features map, the AFS branches are taken from Kaveh et al, 2013 (Figure 2 b). It has been known that this fault system generates some morphotectonics features such as scarps, right lateral offsets and shutter ridges (Figure 4 up to Figure 10). All of these features show that the AFS has two components, one of them is reverse and another is strike slip. In some parts the reverse faults with strike slip component have made the fault scarps (Figure 4 & Figure 5). Where the strike slip component is dominant in comparison with reverse component, this fault system

has produced the shutter ridges and streams offsets (Figure 6 up to Figure 10 & Figure 15). Based on observed displacements at rivers, the dextral displacement is recognized by shear displacement (Figure 6, Figure 9 & Figure 15).

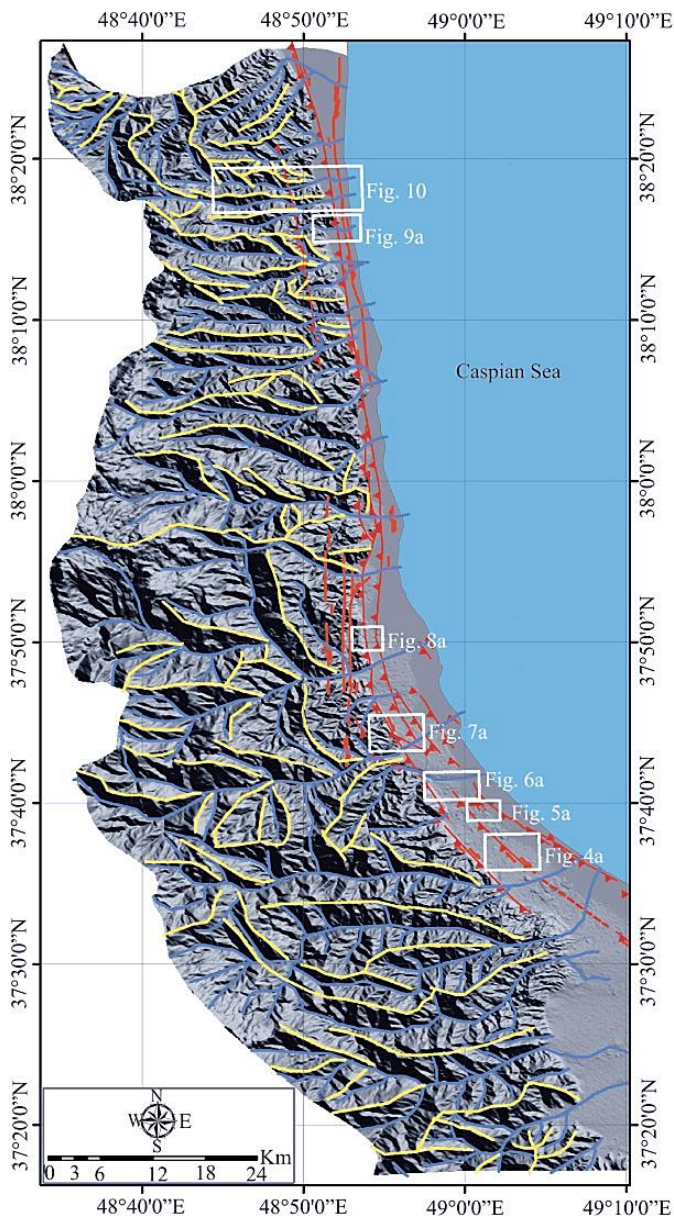


Figure 3: Map of the morphotectonic features observed in Gilan province from DEM30 m ([http://dds.cr.usgs.gov/srtm/version2\\_1/SRTM30//srtm30](http://dds.cr.usgs.gov/srtm/version2_1/SRTM30//srtm30)): yellow lines, blue lines and red lines show crest lines, drainages and fault branches of AFS (Kaveh et al.,2013), respectively. Rectangle enclosed areas are shown in the following figures.

#### **4- KINEMATICS OF ASF**

Kaveh et al., (2013) estimated the dip and rake values of ASF. In this section topographic map created using DEM 10 m along with trigonometric relationships were utilized to estimate the rake values (Figure 11 up to Figure 13). The main focus was on the dextral displacements at the riverbed which were observed at two locations (Figure 6 & Figure 9). Through field investigation, a scarp of 2 m height was identified at 321908/4123101 UTM coordinate whose trend is N 308° (Figure 6). With tracing this trend toward the NW the dextral offset was discerned in the river (Figure 6). On the account of the topographic map, the displacement of this river is estimated to be about  $32 \pm 2$  m horizontally and  $0.6 \pm 0.10$  m vertically (Figure 12). Based on fig.11 and 12 the rake value of this probable segment is estimated to be 2° which is the same as the subsegment number 2 of strike slip segment of the AFS fault at Kaveh et al., (2013).

Field observations revealed a dextral offset located at 313602/4236820 UTM coordinate which is

trending in the direction of N300° (the angle between this probable segment and thrust fault of AFS is 55°). Continuing this trend towards the SE for 300 meters, a scarp of the rural road was observed (Figure 9). Accordingly, based on the topographic map and field estimation, the displacement of this riverbed is estimated to be  $33\pm 2$  m horizontally and  $1.6\pm 0.20$  m vertically (Figure 13). As shown in Figure 11 & Figure 13 the rake of this probable segment is estimated to be 5.2° which is the same as the subsegment number 2 of thrust segment at Kaveh et al., (2013).

## **5- PALAEOSEISMOLOGY**

According to the above discussion and the lack of sufficient information regarding the seismic behavior of the area and the need for assessment of the regional seismic hazard (McCalpin, 2009); we conducted a paleoseismological study on the AFS.

### ***5-1- SITE SELECTION***

Based on what was described in morphotectonics section, there are many difficulties to the process of site selection at the studied area. After taking every aspects of the problem into consideration, some parts of Lisar river natural bank were eventually selected for paleoseismological investigation (Figure 14 & Figure 15). These studied parts of river bank are located at 2 km west of Lisar city at 315138/4203645 (UTM coordinate) with East - West trending longitudinal axis and north -

south facing direction. Abrupt change of alluvium material (Figure 14) content is the main rationale for selection of these parts of river natural bank as it conforms to the faults drawn by Kaveh et. Al (2013) and it is in accordance with the magnetic anomaly number 2 (Figure 15 g) which ultimately leads to the conclusion that the right lateral displacement of the river could be interpreted as AFS movement.

Banks on both sides of the river were excavated two meters deep in order to trace the visible surface evidences to the depth of the ground. Thus, the excavated trenches were 5 meters high, 11 meters long and 1.5 meter wide. As the geological evidences were similar in both riverbanks, due to better peripheral light conditions, the south bank was selected to be logged on a 1/20 scale with a reference grid of 1m<sup>2</sup> square. The findings are interpreted as paleoseismological evidence which includes indications of the vertical fault that sheared Quaternary alluvium (Figure 16).

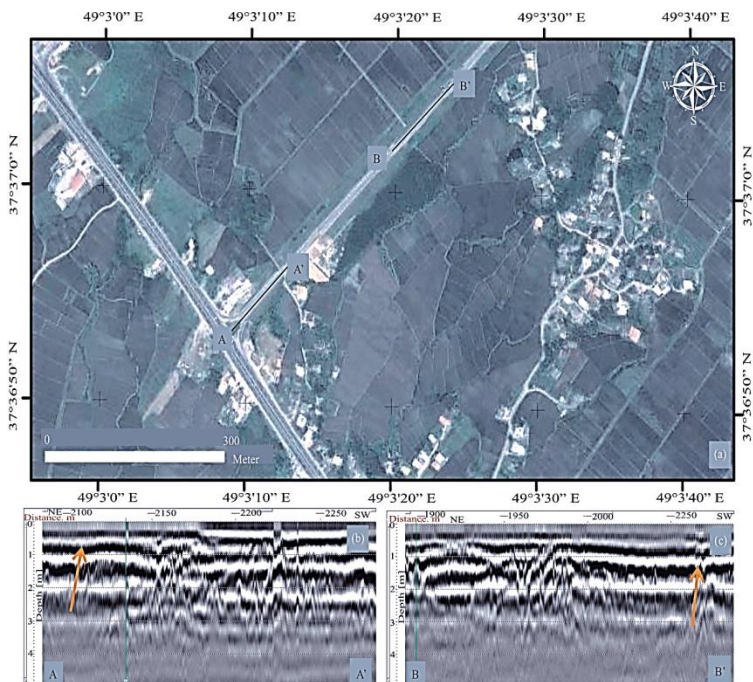


Figure 4: a) The Google Earth image of fault scarp, see fig.3 for locations. The black lines represent the GPR profiles at the fig. b and c. b and c show the GPR profile at A - A' and B-B' lines, respectively. Orange arrows and green lines at b and c represent the base of pavement and vertical anomaly, respectively. The GPR results are taken from Mohammadi Vijeh., (2013).

### 5-2- STRATIGRAPHY AND AGE OF UNITS

Within the excavations of the banks, 2 zones are clearly distinguished, one of them is a clayey zone which is approximately without any clast and another is a

clastic zone along with sand, silt and clay as a matrix (Figure 14). Within the clastic layer, several units can be discerned. The discrepancy of units arises from differences in color, grain size and percentage, stratification state, roundness degree, sorting degree, matrix type and eventually sedimentary environment (McCalpin,2009; Nazari et al, 2009; Nazari et al,2011; Ritz et al,2012; Foroutan et al,2012) (Figure 16). Based on the mentioned parameters, 13 different units have been detected in the riverbank (Figure 16 b). The uppermost layer of the bank is made of artificial soil (unit13). Units 1,2,4-6,8-10 and 12 contained almost the same size of pebbles. In general, units 3 and 11 are made of clay size aggregates. Meanwhile, they have smaller pebbles in some parts, such as a lentoid layer. Unit 7 is attributed to turbidity current flow; consequently, it contains pebbles as much as boulder size rocks (Figure 16).

Paleoseismological Analysis along the Astara Fault System (Talesh Mountains, North Iran)

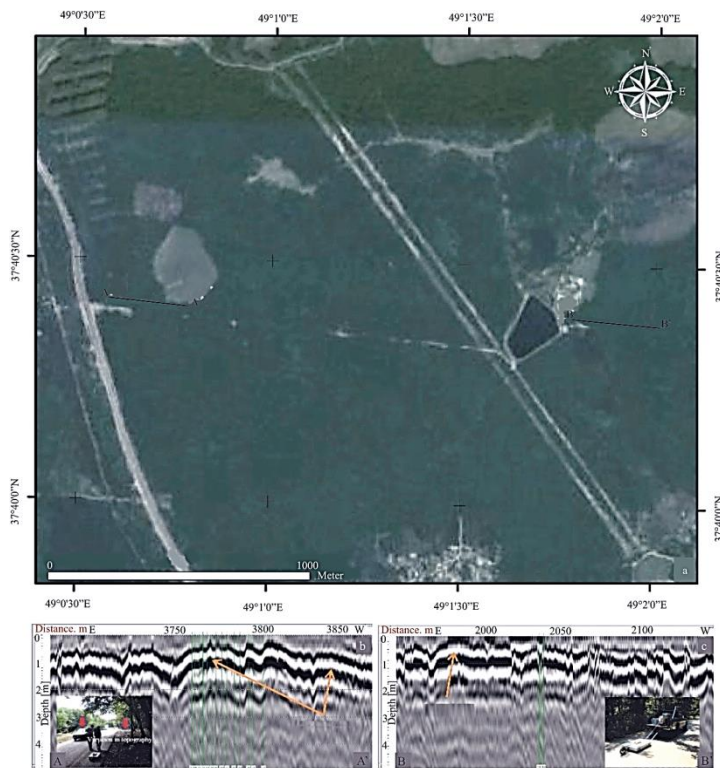


Figure 5: a) The Google Earth image of fault scarp, see fig.3 for locations. The black lines represent the GPR profiles at the fig. b and c. b and c show the GPR profile at A - A' and B-B' profiles, respectively. Orange arrows and green lines at b and c represent the base of pavement and vertical anomaly, respectively. The GPR results are taken from Mohammadi Vijeh., (2013).

## Paleoseismological Analysis along the Astara Fault System (Talesh Mountains, North Iran)

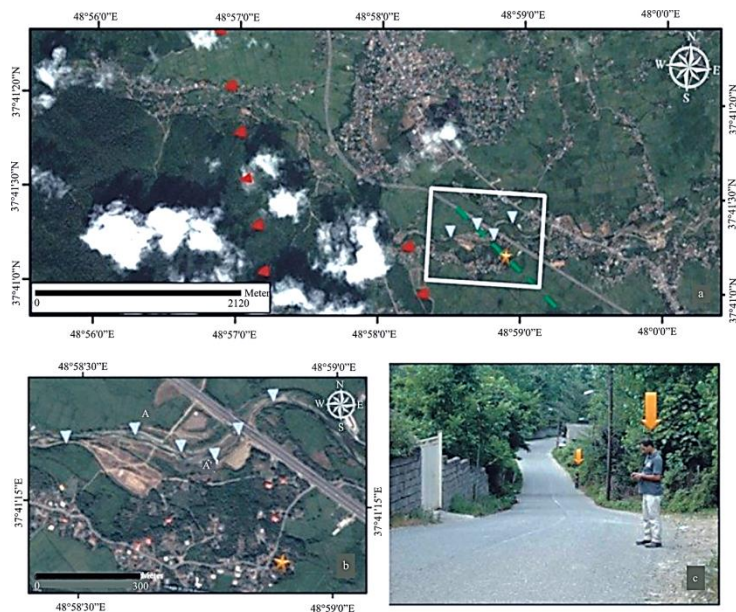


Figure 6: a) Google earth view of the scarp and offset of the river, see fig.3 for location. Red triangles denote the thrust faults segments (Kaveh et al, 2013). Dash green line represents the probable segment of AFS. Orange star denotes the abrupt change in elevation at fig. c, this scarp has N308 trend. The light blue triangles and A-A' represent the right lateral offset of the river ( $32\pm 2$  m). white rectangle denotes the fig. b. b) Closer view of right lateral offset of the river (light blue arrows) on the Google earth image and scarp (orange star). c) The field photo at the star location in fig. 6a and 6b.

Table 1: The results of  $^{14}\text{C}$  dating tests of organic materials

Laboratory N°	Reference	Nature	$\delta^{13}\text{C}$	Age conv. BP	Intervalle of Calibrated Date	Mean Date	Median Date
			(‰)		(Cal BP)	(Cal BP)	(Cal BP)
SacA36974/Gif-13066	ASFT1-C1	Charcoal	-23.83	23170 ± 240	27808-27032	27430±197	27444
SacA36975/Gif-13067	ASFT1-C2	Charcoal	-22.30	28400 ± 290	33202-31515	32346±443	32335
SacA36976/Gif-13068	ASFT1-C3	Charcoal	-30.72	10995 ± 50	13000-12730	12861±75	12855
SacA36977/Gif-13069	ASFT1-C4	Charcoal	-23.73	11005 ± 50	13008-12734	12872±75	12868
SacA36978/Gif-13071	ASFT1-C5	Charcoal	-20.10	11065 ± 45	13059-12799	12927±71	12931
SacA36979/Gif-13072	ASFT1-C6	Charcoal	-27.47	11045 ± 50	13055-12772	12909±74	12910

The evidence of paleoearthquakes were observed in units 1 upto 9, in which changes of orientation in the grains were clear and relative displacement was apparent in adjacent layers; accordingly, unit 4 is made out of colluvium wedge (Figure 16). Based on this evidence, 3 to 4 paleoearthquakes could be identified. In this research six Carbon samples were obtained from the units 3,11 and 11b, two samples each (Figure 16 b,Figure 19 and Table 1). These charcoal samples were properly prepared following a standard procedure (Délibrias, 1985) at the LSCE Laboratory (Gif/Yvette). Charcoal samples were treated using the ABA (Acid: Base: Acid) method, then combusted at 900°C, and the radiocarbon activity was finally measured using AMS facilities of LMC14 (ARTEMIS) at Saclay (see for example Ollivier et al., 2015 for more technical details). Conventional  $^{14}\text{C}$  ages are expressed in years before present (BP), with 1s error. Ages were calibrated using OxCal v4 2.3 Bronk Ramsey and Lee, 2013: r5 IntCal 13 atmospheric curve (Reimer et al., 2013). The  $\delta^{13}\text{C}$  values used for conventional age calculation are obtained from accelerator measurement and include carbon isotope fractionation due to graphitization and presence of ion beams during measurements. They have no paleoenvironmental significance (Figure 19, Table 1). Results reported in Table 1 show that the four samples (ASFT1-C3 to C6) represent the same event (mean value  $11,028 \pm 49$   $^{14}\text{C}$  years BP, median date 12,893 cal BP). The age of stratigraphic units is different, considering that their time of origin is ranging from older than

28,400 ± 290 BP to younger than 10,995 ± 50 BP. The oldest age ASFT1-C2 (28,400 ± 290) is related to the units located at the bottom of the bank (units 1 and 2). The ages of units 3 to 11 fall in the range of 28,400 ± 290 BP to 10,995 ± 50 BP. Unit 12 and 13 are younger than 10,995 ± 50BP (Figure 19 and Table 1).

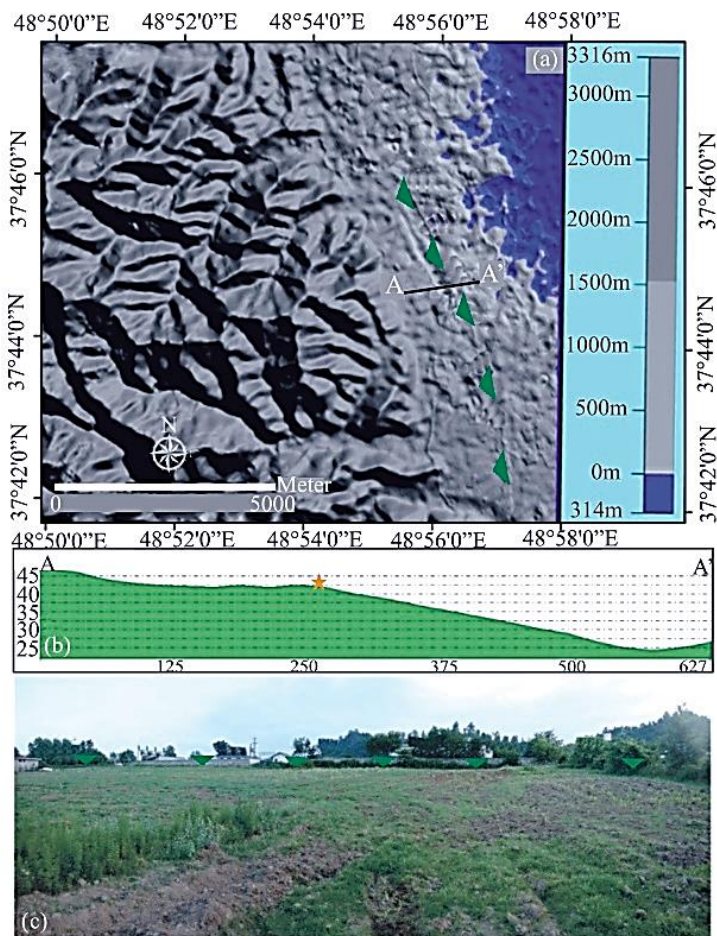


Figure 7: a) DEM 30 m view at 317868/4178924 UTM coordinate, see fig.3 for location. Light green triangles, black line and orange star denote the scarp trend, longitudinal profile and location of the abrupt change in elevation, respectively. b) Longitudinal profile at A-A' line (see image a

for location). c) The field photo. The light green triangles represent the fault scarp.

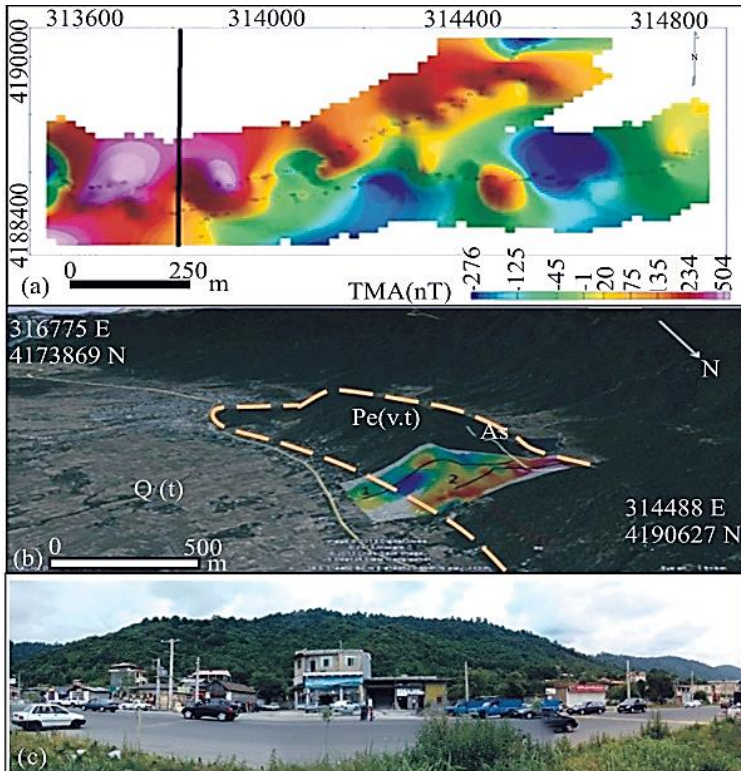


Figure 8: a) Diagram depicting The magnetic anomaly at shutter ridge. The black line shows the ASF fault. b) The magnetic anomaly Diagram on a Google earth image. The black and white lines along with orange dash line denote the scan line, ASF and shutter ridge, respectively. Q (t) and Pe (v.t) are quaternary alluvium and andesitic tuff, respectively (Asadi, 2013).c) the field photo of the shutter ridge.

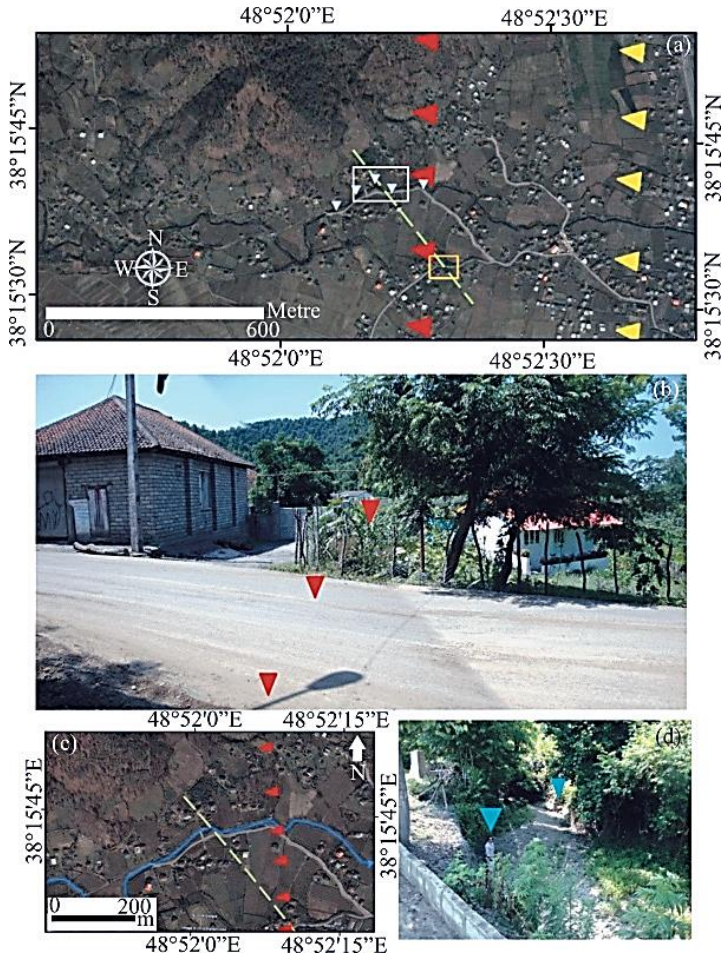


Figure 9: a) Google earth view at scarp and offset of river. The yellow, red, blue triangles and dash green line denote the strike slip, thrust, right lateral offset of river and probable segments of AFS, respectively. The orange and white rectangles represent fig. b and c, respectively. See fig.3 for locations. b) The field photo of scarp, the red triangles denote

the scarp and abrupt change of elevation. c) The closer view at the right lateral offset. red triangles, green dash line, blue line and A-A' represent the thrust fault, probable segments of AFS, river and river offset ( $33\pm 2\text{m}$ ). d) The field photo of right lateral displacement in the river.



Figure 10: see fig. 3 for location. In this field photo two points are shown, one of them is dextral offset at river that is represented with blue arrows and another is shutter ridge feature that is denoted with red arrows. The red dash line with sense motion shows the probable of ASF segments.

### ***5-3- SEISMIC EVENTS***

Based on resemblance of units' materials, retracement of the displacements and reconstruction of the bank log, three or four event horizons are identified as evidence of three or four seismic events that ruptured the ground surface. The evidences of these seismic events are labeled as EvI up to EvIV from the youngest to the oldest, respectively. Regarding the uppermost units, a part of unit 11 was eroded under influence of unit 12 deposition, for which two scenarios are suggested. The following subsections will discuss each of these scenarios.

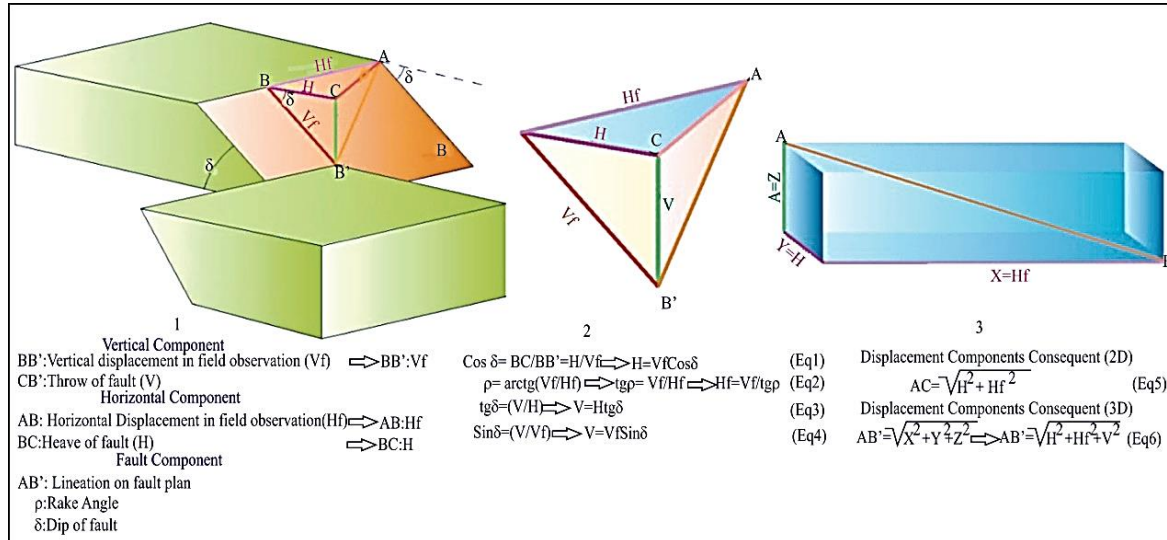


Figure 11: Calculation of trigonometric relationships.  $V_f$ =the vertical offset measured on the riverbank,  $H_f$ = the horizontal displacement stems from the  $V_f$  and different rake values,  $V$  and  $H$  respectively representing the throw and heave of fault,  $\rho$ =rake,  $\delta$ =dip of fault,  $AC$ = resultant displacement component in two and three dimensions.

Paleoseismological Analysis along the Astara Fault System (Talesh Mountains, North Iran)

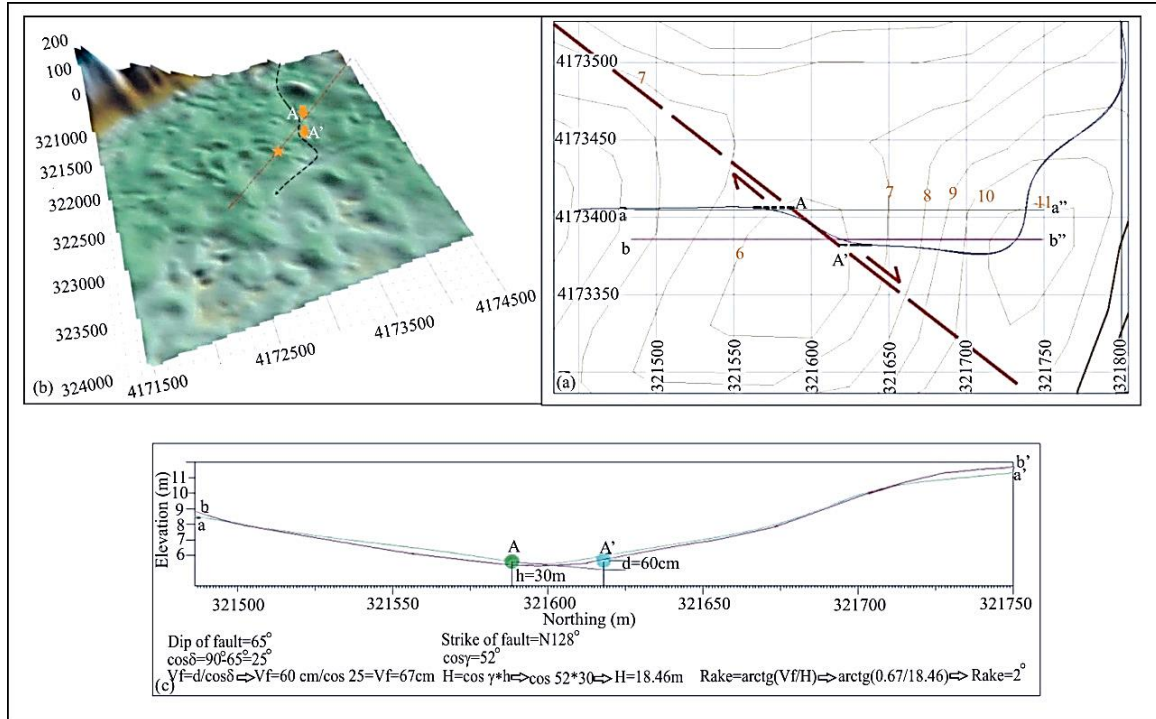


Figure 12: a) The topographic map that stems from Dem 10 m at the dextral displacement of river. The green, magenta, dark blue and dash red lines show the profile survey at fig. c, river and probable fault segment, respectively. The vertical interval of each counter is 1 meter. b) The 3D modeling of the studied area. c) The estimation of rake value based on fig. 10.

Paleoseismological Analysis along the Astara Fault System (Talesh Mountains, North Iran)

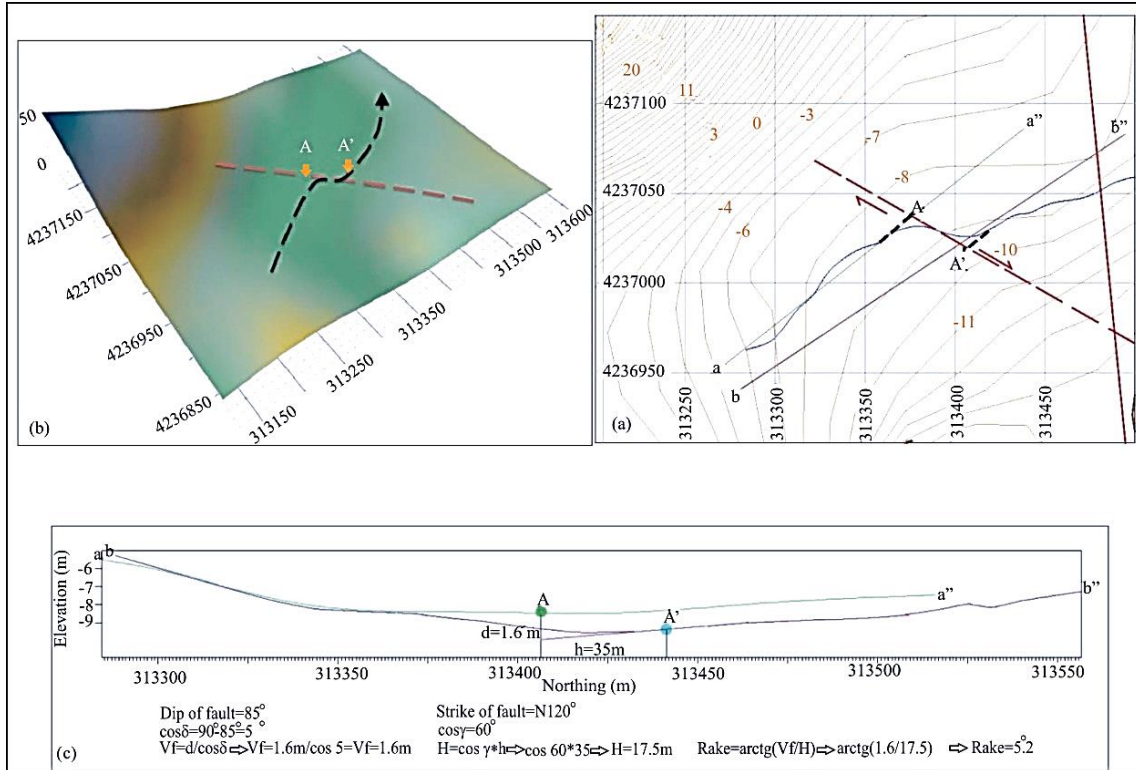


Figure 13: a) The topographic map that stem from Dem 10 m at the dextral displacement of the river. The green, magenta, dark blue and dash red lines show the profile survey at fig. c, river and probable fault segment, respectively. The vertical interval of each counter is 1 meter. b) The 3D modeling of the studied area. c) The estimation of rake value based on fig.10.

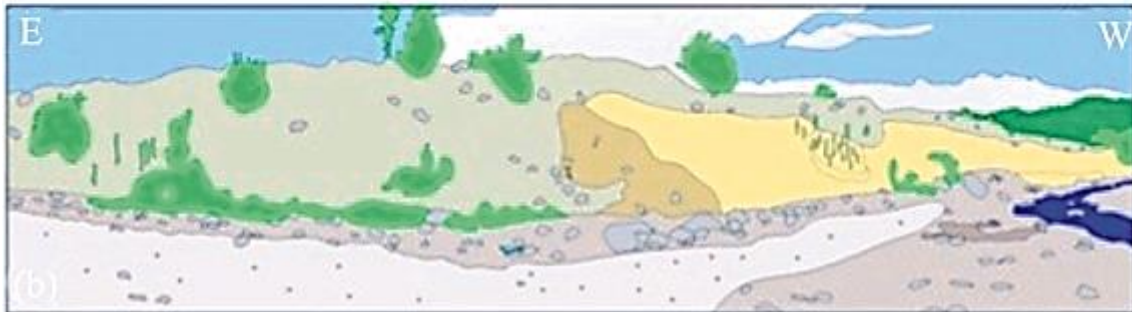


Figure 14: a) Field photo of the south bank. b) Corresponding cartoon drawing of the bank. Yellow, brown and grey parts in drawing sketch are indication of the clay part and the clastic layer, respectively.

### **5-3-1- Scenario A**

#### **(1) EvI**

The latest earthquake whose evidence is identified on the lisar river bank was determined to have occurred before  $10995 \pm 50$  Cal BP. The absence of seismic activity since  $10995 \pm 50$  Cal BP up to now (table 1) is not in accordance with morphotectonical and seismic findings. Hence, we postulate that an earthquake occurred after deposition of the unit11 and before disposition of the unit 12 whose age is the same as EvI in the scenario B. The corroboration of this assumption is difficult, because the sedimentation of Unit 12 led to erosion of the top of Unit 11 layer. As a result, the evidence of this event has been removed (Figure 17, Figure 19 & Figure 20, Table 2).

#### **(2) EvII**

Fault branches F1 and F3 have continued up to the underneath of unit 9 erosion surface and displacement along these faults at unit 5 up to unit 8 is calculated to be about 0.19 m while it is possible that layers from unit 9 onwards had undergone displacement just as well but its evidences have been removed due to erosion. As a result, it can be assumed that Unit 9 is an event horizon and the age of this event is less than  $23,179 \pm 240$  BP and more than  $11,065 \pm 45$  BP (Table 2). However, the evidence of this event was eroded by

sedimentation of upper units (Figure 17, Figure 19 & Figure 20, Table 1 & Table 2).

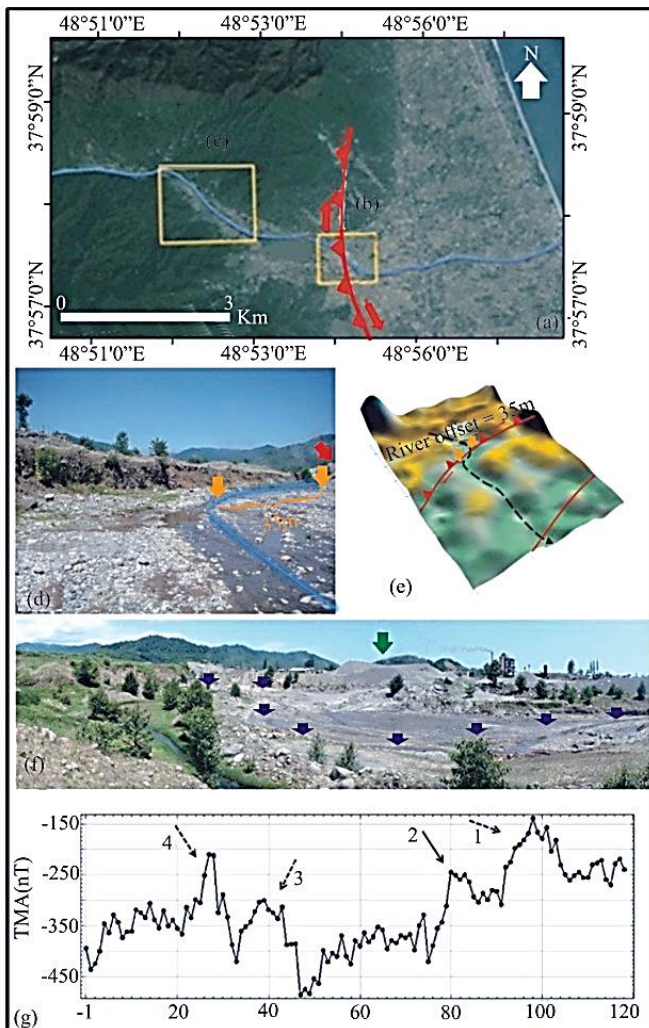


Figure 15: a) A Google Earth image of Lisar river in which the AFS branch is shown, see fig. 3 for location. Rectangles b and c denote on d and f figures, respectively. d) field picture of right lateral displacement that is represented with rectangle b in image a. solid blue line shows recent river flow and displacement amount is shown with orange color. e) 3D model of rectangle b, dash black line is representative of the river and red line with triangle is an indication of AFS branch (reverse fault with right lateral component). f) field picture of rectangle c in image a, blue arrow shows right lateral displacement of river flow and green arrow is showing the sand mine. g) Diagram depicting magnetic anomaly of Lisar river which is showing 4 anomalies, anomaly number 2 conforms with AFS branch which is drawn by Kaveh et al, 2013 (Asadi, 2013).



### (3) EvIII

Evidence corroborating this event is the cut through the colluvium wedge (unit 4) which was created as a result of an earlier event (EvIV). therefore, the time of its occurrence is after deposition of unit 3 and subsequent deposition of unit 4 (later than  $23,170 \pm 240$  BP and sooner than  $11,065 \pm 45$  BP) (Figure 17, Figure 19 & Figure 20, Table 2).

### (4) EvIV

The colluvium wedge (unit4) was created as a result of this event which had the movement of F4 fault branch as its main seismic source. Unlike Units 3 and 5, Unit 4 is consisted of clast and clay as a matrix while unit3 is made of clay with a lentoid layer of debris and unit 5 is made of clasts and sand as a matrix. Regarding the Unit 4, we assumed that this unit arose from mixture of Unit 3 and another unit that was eroded by deposition of Unit 5. Consequently, we defined the Unit 3a that was consisted of clasts and clay as a matrix. To reconstruct it, we assumed its thickness to be about the average thickness of Unit 4. This event generated 0.15 m vertical displacement at Units 3 and 3a (Figure 17, Figure 19 & Figure 20, Table 2).

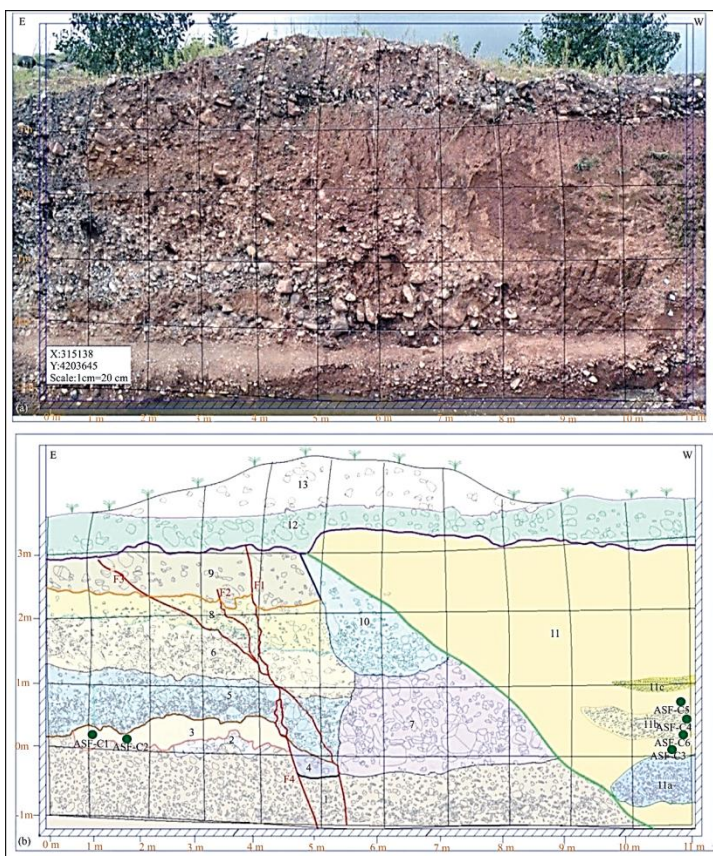


Figure 16: a) photomosaic of Lisar River wall (see Fig. 2 for location). b) Respective log, with labels marking the stratigraphic units.

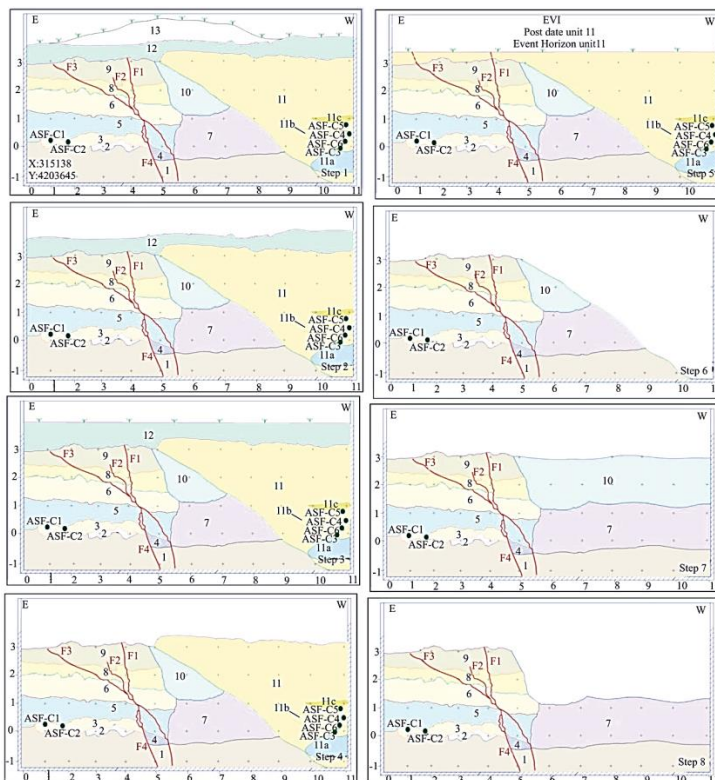
Faults are shown with red lines. Colored lines correspond to bedding of sedimentation layers. Labeled green circles are showing the location of the C<sup>14</sup> sampling. The results of dating procedure of the Samples ASF-C1, ASF-C2, ASF-C3, ASF-C4, ASF-C5 and ASF-C6 are  $23,170 \pm 240$  conv. BP,

28,400 ± 290 conv. BP, 10,995 ± 50conv. BP 11,005 ± 50 conv. BP, 11,065 ± 45 conv. BP and 11,045 ± 50conv BP, respectively. Detailed stratigraphic explanations of units' contents: unit 1: Light brown to light gray alluvial deposit, well stratified, 90-95% clasts (prevalent size: 0.5-7 cm, in some parts 15-20cm) Medium sorted, sub angular to sub-rounded, the matrix is consisted of silt, clay and gray sand. Unit2: Dark Gray alluvial loss deposit as a lentoid layer: none stratified, 60% clasts (prevalent size: 0.5-10cm, rarely 20cm) sub-rounded to rounded and poor sorted: the matrix is mostly consisted of sand. Unit3: Light brown well consolidated alluvial deposit: 5% clasts as a lentoid layer (prevalent size: 0.5-2 cm) poorly stratified in some parts, sand as a lentoid layer at the bottom of unit, the matrix is consisted of silt and clay. Unit4: Light brown colluvium wedge deposit, 30% clasts (prevalent size: 0.5-3 cm) none stratified, sub-angular to sub-rounded, the matrix is consisted of silt and clay. Unit5: Gray alluvial deposit: well stratified, 90% clasts (prevalent size: 0.5-7cm, in some parts 20-40cm) rounded to sub-rounded and medium sorted, the matrix is consisted of sand, silt and clay. Unit6: Gray to light brown alluvial deposit, fairly stratified, 75% clasts (prevalent size: 0.5-10 cm) angular to sub-rounded and poorly to medium sorted, the matrix is consisted of sand, silt and clay. Unit7: Light brown torrential deposit, none stratified, 60% clasts (prevalent size: 0.5-30 cm mainly, in some parts 50-70 cm), Grain roundness: sub-angular to sub-rounded, none sorted, the matrix is consisted of clay, silt and sand. Unit8: Light brown to gray alluvial deposit: fairly stratified, 30% clasts (prevalent size: 0.5-7cm, in some parts 15-25cm), sub-rounded, poorly sorted, the matrix is consisted of sand, silt and clay. Unit9: huffish to light brown alluvial deposit, roughly stratified, 60% clasts (prevalent size: 0.5-10cm, in some parts 20-25cm), sub-rounded, poorly sorted,

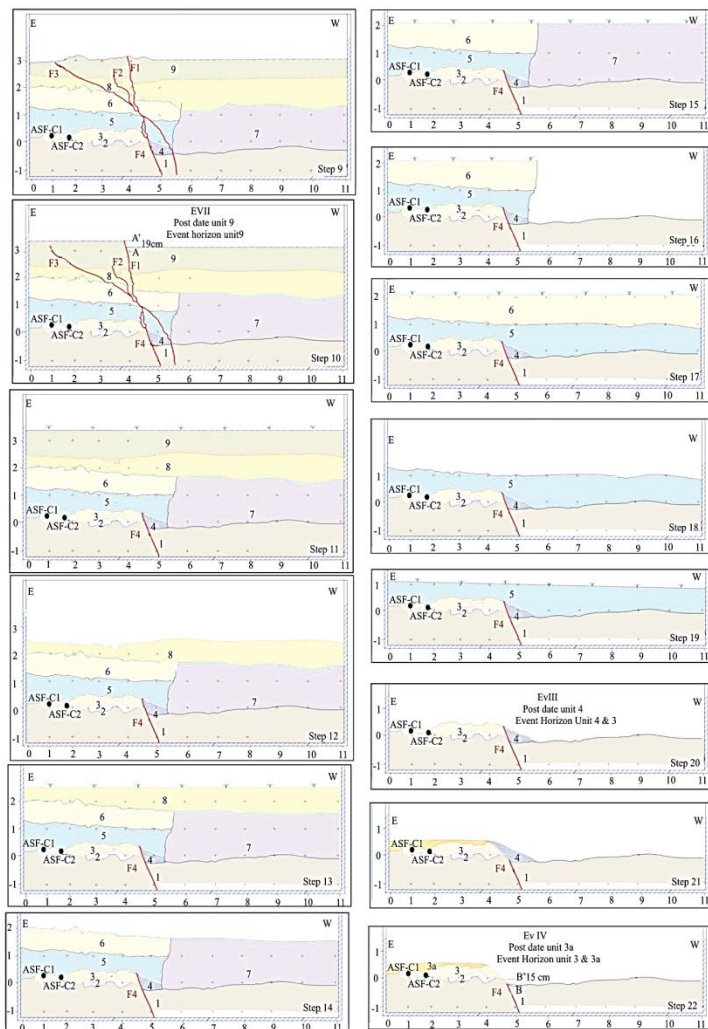
the matrix is consisted of sand, clay and silt. Unit10: Brown mud flow deposit, 75% clasts (prevalent size: 0.5-10cm, the maximum clast size 35 cm), none stratified (oriented clasts), sub-angular to sub- rounded, poorly sorted, unconsolidated to consolidated clay from base to top, the matrix is consisted of silt and sand. Unit11: Dark brown pond deposit, none stratified, 5% clasts (prevalent size: 0.5- 1cm, rarely 15 cm) compacted clay, include a gravel layer of lentoid shape with bioturbation. Unit11a: Light gray alluvial deposit lentoid shape, well stratified, 90% clasts (prevalent size: 0.5- 10cm, rarely 15 cm) sub-angular to sub-rounded, poorly sorted, the matrix is consisted of clay, sand and silt. Unit11b: Light brown alluvial deposit lentoid shape, roughly stratified, 80% clasts (prevalent size: 0.2-2.5cm with maximum clast size as 6 cm), sub-angular to sub-rounded, medium sorted, the matrix is consisted of silt, clay and sand. Unit11c: Same as 11 b. Unit12: Gray alluvial deposit, roughly stratified, 95% clasts (prevalent size: 0.5-15 cm, rarely 40 cm), sub-angular to sub-rounded and poorly sorted, the matrix is consisted of clay, silt and sand. Unit13: artificial soil angular to sub-rounded, the matrix is consisted of silt, clay and gray sand. Unit2: Dark Gray alluvial loss deposit as a lentoid layer: none stratified, 60% clasts (prevalent size: 0.5-10cm, rarely 20cm) sub-rounded to rounded and poor sorted: the matrix is mostly consisted of sand. Unit3: Light brown well consolidated alluvial deposit: 5% clasts as a lentoid layer (prevalent size: 0.5-2 cm) poorly stratified in some parts, sand as a lentoid layer at the bottom of unit, the matrix is consisted of silt and clay. Unit4: Light brown colluvium wedge deposit, 30% clasts (prevalent size: 0.5-3 cm) none stratified, sub-angular to sub-rounded, the matrix is consisted of silt and clay. Unit5: Gray alluvial deposit: well stratified, 90% clasts (prevalent size: 0.5-7cm, in some parts 20-40cm) rounded to sub-rounded and

medium sorted, the matrix is consisted of sand, silt and clay. Unit6: Gray to light brown alluvial deposit, fairly stratified, 75% clasts (prevalent size: 0.5-10 cm) angular to sub-rounded and poorly to medium sorted, the matrix is consisted of sand, silt and clay. Unit7: Light brown torrential deposit, none stratified, 60% clasts (prevalent size: 0.5-30 cm mainly, in some parts 50-70 cm), Grain roundness: sub-angular to sub-rounded, none sorted, the matrix is consisted of clay, silt and sand. Unit8: Light brown to gray alluvial deposit: fairly stratified, 30% clasts (prevalent size: 0.5-7cm, in some parts 15-25cm), sub-rounded, poorly sorted, the matrix is consisted of sand, silt and clay. Unit9: huffish to light brown alluvial deposit, roughly stratified, 60% clasts (prevalent size: 0.5-10cm, in some parts 20-25cm), sub-rounded, poorly sorted, the matrix is consisted of sand, clay and silt. Unit10: Brown mud flow deposit, 75% clasts (prevalent size: 0.5-10cm, the maximum clast size 35 cm), none stratified (oriented clasts), sub-angular to sub- rounded, poorly sorted, unconsolidated to consolidated clay from base to top, the matrix is consisted of silt and sand. Unit11: Dark brown pond deposit, none stratified, 5% clasts (prevalent size: 0.5- 1cm, rarely 15 cm) compacted clay, include a gravel layer of lentoid shape with bioturbation. Unit11a: Light gray alluvial deposit lentoid shape, well stratified, 90% clasts (prevalent size: 0.5- 10cm, rarely 15 cm) sub-angular to sub-rounded, poorly sorted, the matrix is consisted of clay, sand and silt. Unit11b: Light brown alluvial deposit lentoid shape, roughly stratified, 80% clasts (prevalent size: 0.2-2.5cm with maximum clast size as 6 cm), sub-angular to sub-rounded, medium sorted, the matrix is consisted of silt, clay and sand. Unit11c: Same as 11 b. Unit12: Gray alluvial deposit, roughly stratified, 95% clasts (prevalent size: 0.5-15 cm, rarely 40 cm), sub-angular to sub-

rounded and poorly sorted, the matrix is consisted of clay, silt and sand. Unit13: artificial soil.



## Paleoseismological Analysis along the Astará Fault System (Talesh Mountains, North Iran)



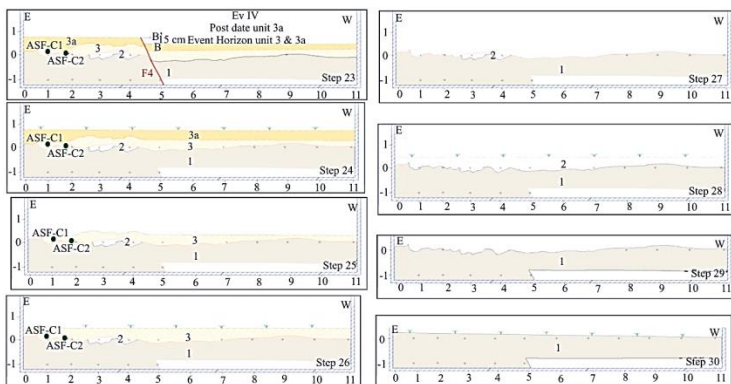


Figure 17: Schematic views of Lisar riverbank log based on the scenario A form the present day (Step1) back to before the oldest event occurrence (Step 30).

The riverbank log has been simplified for the sake of clarity and ease of comprehension. Dashed colored lines show surmised ground surface before the erosion. Step 1: present day situation. Step 2: elimination of the unit 13 and reaching the erosion surface of the unit 12 (after EV I). Step 3: restoration of the ground surface before erosion of the unit 12 (after EV I). Step 4: elimination of the unit 12 and reaching the erosion surface of the units 11 and 9 (after EV I). Step 5: restoration of the ground surface before erosion of the unit 11 and reaching the EVI time of occurrence (event horizon, unit11). Step 6: elimination of the unit 11 (after EVII, before EVI). Step 7: restoration of the unit 7 and 10 before erosion which was induced by deposition of the unit 11 (after EVII, before EV I). Step 8: elimination of the unit 10 (after EVII, before EVI). Step 9: restoration of the unit 8 and 9 before erosion induced by deposition of unit 10 (after EVII, before EVI). Steps 10: restoration of the unit 9 before erosion and after occurrence of EVII which is showing a vertical

displacement of about 0.19 meter originated from F1 fault branch activity. Step 11: restoration of the displacement before EVII (after EVIII, before EVII). Step 12: elimination of the unit 9 and reaching the erosion surface of the unit 8 (after EVIII, before EVII). Step 13: restoration of the unit 8 before erosion (after EVIII, before EVII). Step 14: elimination of the unit 8 and reaching the erosion surface of the units 6 and 7 (after EVIII, before EVII). Step 15: restoration of the units 6 and 7 before erosion (after EVIII, before EVII). Step 16: elimination of the unit 7 (after EVIII, before EVII). Step 17: restoration of the units 5 and 6 before deposition of the unit 7 (after EVIII, before EVII). Step 18: elimination of the unit 6 and reaching the erosion surface of the unit 5 (after EVIII, before EVII). Step 19: restoration of the unit 5 before erosion. Step 20: elimination of the unit 5 and reaching the occurrence time of the EVIII that sliced the colluvium wedge (the unit 4). Step 21: restoration of the unit 4 and the unit 3a before EVIII and after EVIV. Step 22: elimination of the unit 4 and reaching the EV IV which is showing a vertical displacement of about 0.15 meter originated from F4 fault branch activity. Step 23: restoration of the unit 3 and 3a after occurrence of EV IV. Step 24: restoration of the unit 3, 3a and the displacement induced by the event (before EV IV). Step 25: elimination of the unit 3a and reaching the erosion surface of the unit 3 (before EV IV). Step 26: restoration of the unit 3 before erosion (before EV IV). Step 27: elimination of the unit 3 and reaching the erosion surface of the units 1 and 2 (before EV IV). Step 28: restoration of the unit 2 before erosion (before EV IV). Step 29: elimination of the unit 2 and reaching the erosion surface of the unit 1 (before EV IV). Step 30: restoration of the unit 1 before erosion (before EV IV).

### **5-3-2- Scenario B**

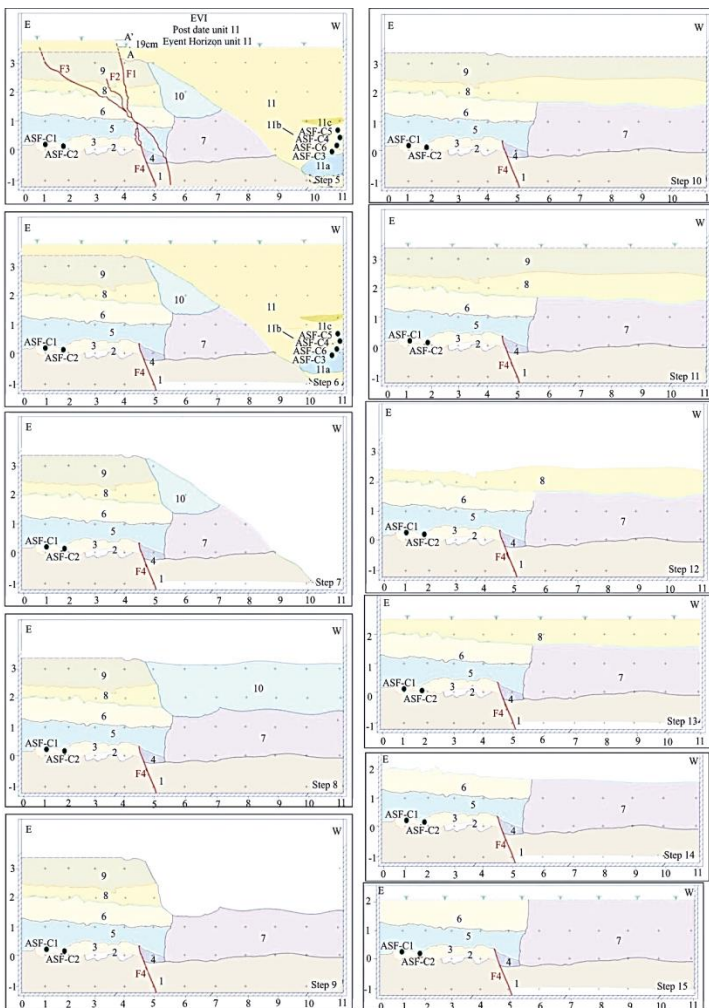
#### **(1) EvI**

Presuming the F1 and F3 fault branches continued above the unit 9, it could be assumed that those faults sliced the unit 11 and displaced it 0.19 m vertically, similar to the displacement which is measured from unit 5 up to unit 8. In order to accept this hypothesis, unit 11 should be considered as event horizon of this event. The latest dating test result is 12,855 cal BP (ASFT1-C3, table 2) which respective sample is taken from 2.66 meters under erosion surface of unit 11. If we consider the paleoclimatic conditions of the studied region to be the same as those of the south Caspian basin (Leroy et al.,2013), the deposition rate could be assumed to be approximately equal to that of the Baliran section located at the shore of south east Caspian basin which is 0.27 mm/year (Antoine et al.,2006). Based on this deposition rate, the age of this event could be estimated to be about 3 ka. However, due to erosion induced by the deposition of unit 12, this situation does not exist at the present time (Figure 18,Figure 19 &Figure 20; Table 1).

#### **(2) EvII & EvIII**

Refer to EVIII and EV IV at Scenario A (Figure 18,Figure 19 &Figure 20; Table 2).

# Paleoseismological Analysis along the Astara Fault System (Talesh Mountains, North Iran)



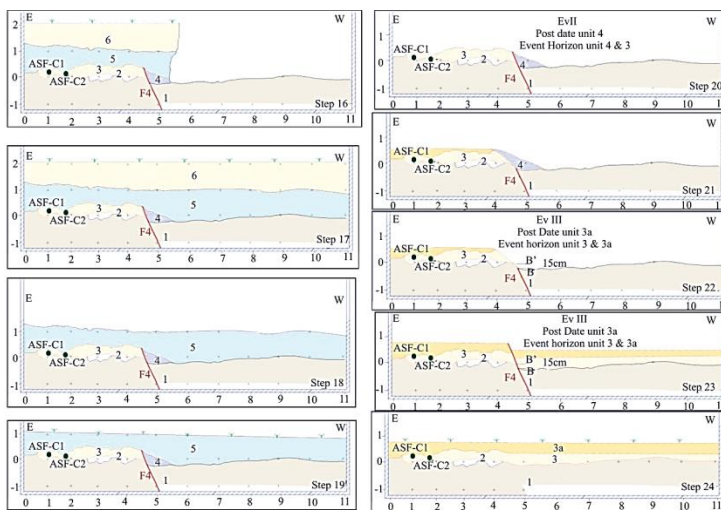


Figure 18: Schematic views of Lisar riverbank log based on the scenario B.

The restoration process from step 1 up to step 4 is the same as the scenario A. Step 5: restoration of the ground surface and the displacement induced by EVI before erosion of the unit 11, occurrence of EV I which is showing a vertical displacement of about 0.19 meter originated from F1 fault branch activity (event horizon unit11). Step 6: restoration of the unit 11 and the displacement induced by the event occurred before EVI. Step 7: elimination of the unit 11(after EVII, before EVI). Step 8: restoration of units 7 and 10 before erosion which was resulted from deposition of the unit 11 (after EVII, before EVI). Step 9: elimination of the unit 10 (after EVII, before EVI). Step 10: restoration of the units 8 and 9 before erosion resulted from deposition of unit 10 (after EVII, before EVI). Step 11: restoration of the unit 9 before erosion. Step 12: elimination of the unit 9 and reaching the

erosion surface of the unit 8 (after EVII, before EVI). Step13: restoration of the unit 8 before erosion (after EVII, before EVI). Step 14: elimination of the unit 8 and reaching the erosion surface of the units 6 and 7 (after EVII, before EVI). Step 15: restoration of the units 6 and 7 before erosion (after EVII, before EVI). Step 16: elimination of the unit 7(after EVII, before EVI). Step 17: restoration of the units 5 and 6 before deposition of the unit 7 (after EVII, before EVI). Step 18: elimination of the unit 6 and reaching the erosion surface of the unit 5 (after EVII, before EVI). Step 19: restoration of the unit 5 before erosion. Step 20: elimination of the unit 5 and reaching the occurrence time of EVII that sliced the colluvium wedge (the unit 4). Step 21: restoration of the units 4 and unit 3a before EVII and after EVIII. Step 22 elimination of the unit 4 and reaching the occurrence time of the EV III which is showing a vertical displacement of about 0.15 meter originated from F4 fault branch activity. Step 23: restoration of the units 3 and 3a after occurrence of EV III. The restoration of steps 24 to step 30 are the same as the scenario A.

## **6- SEISMIC BEHAVIOURS**

### ***6-1- MAGNITUDE OF PALEOEARTHQUAKES***

Based on the vertical displacements measured along the faults, the horizontal component was measured by the usage of the trigonometric equations also the—minimum, average and maximum rake values, (Kaveh et al.,2013) were calculated based on morphotectonical analysis. Eventually the total offsets per event were

estimated. These offsets were in the range of 1.2 m to 2.1 m (Table 1). In order to estimate the moment magnitude  $M_w$ , the empirical relation of Wells and Coppersmith (1994) has been used for all of the fault types, when the expected moment magnitude is in a range of 6.7 to 7.2. Assuming that a strong earthquake can rupture a 54 km of the AFS length, based on Wells and Coppersmith 1994 equation, a 7.2 magnitude earthquake produces a surface rupture length of 54 km (Figure 10, Table 2).

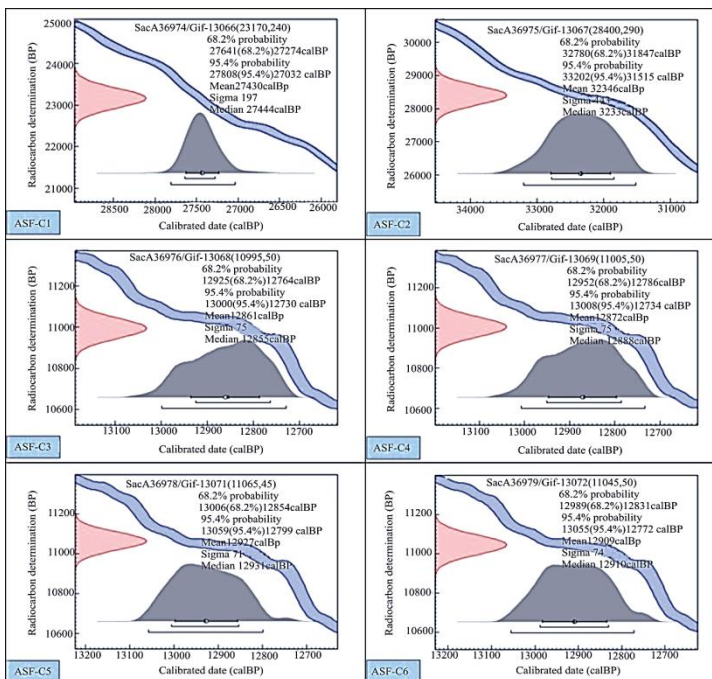


Figure 19: Probability distribution based on results of six  $^{14}\text{C}$  dating samples tests.

The vertical axes are representing the radio carbon concentration in the previous years before the present time and horizontal axes are showing the annual calendar based on the test results. the blue double-line curve, red and gray filled curves respectively represent radiocarbon amount estimation (positive and negative limits with standard deviation), residual radiocarbon concentration in the samples and the possible age based on each sample (the highest elevation of gray filled curves is close to the sample age). Labelled blue rectangle is showing the name of the sample (see fig. 3 for location).

## ***6-2- RECURRENCE INTERVALS OF EARTHQUAKE***

Based on the paleoseismological findings and results of dating tests, it is concluded that the Lisar riverbank were hit by three or four earthquakes which produced surface ruptures after 27,444 cal BP (dating test result) up to 3 ka ago (based on estimated age of EvI at scenario B, Figure 16 up to Figure 19). The erosion process has made the youngest events unrecognizable. As a result, considering three or four events, based on observations and available date test results, the age of the oldest event (EvIV and EvIII at scenarios A and B, respectively (Figure 16 & Figure 17)) is not clear and our findings show that it occurred before 27,444 cal BP, the

average recurrence time was measured to be  $7,119 \pm 1017$  years.

### ***6-3- ELAPSED TIME***

If we consider that the youngest event had ruptured the unit 11 (Ev1 at scenarios A and B), which was removed by erosion, and the deposition rate of the Lisar riverbank is similar to the Baliran deposition, the minimum elapsed time is therefore determined to be about 3ka. However, if we assume that the last event occurred before  $10,995 \pm 50$  cal Bp, EvII at scenario A, the maximum elapsed time is therefore  $10,995 \pm 50$  (Figure 16 & Figure 17 and Table 1).

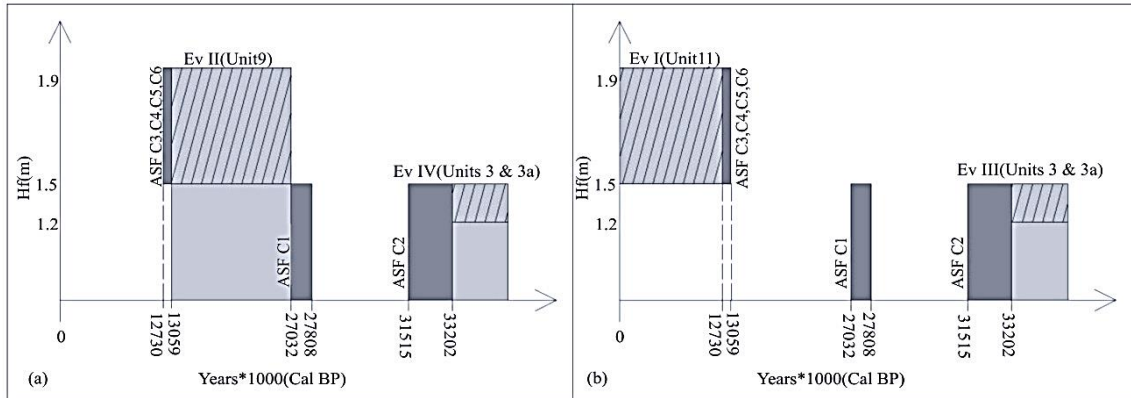


Figure 20: The graph shows the horizontal offsets projected on earth Hf versus the median age (Cal BP).

Dark gray boxes show the age based on  $^{14}\text{C}$  samples. Light gray boxes show, our interpretations of the time windows during which the events occurred. The oblique gray line bands define the minimum and maximum values of offsets. The dash gray lines show the age based on ASF3 up to ASF6. A) Representation of scenario A. B) Representation of scenario B and the age of EvI which is calculated based on the depositional rate by Antoin et al.,2006.

## 7- CONCLUSIONS

Based on paleoseismological research carried out on the Lisar riverbank, two scenarios could be considered. The scenario A is based on 4 events and scenario B has 3 events through which the surface of the studied region was ruptured. Due to The erosion process, the youngest events could not be clearly recognized. considering the depositional rate of the lisar riverbank to be the same as the Baliran depositional rate, the occurrence time of the youngest event at both of the scenarios is estimated to be 3ka ago. The Lisar riverbank has two differentiable displacements. One of them is 0.19m induced by EvII based on scenario A, or EvI based on scenario B and another is 0.15 m induced by EvIII and EvIV based on scenarios A and B, respectively. With regard to these vertical displacements and using the trigonometric relationships as well as the rake values, the horizontal components were measured, then total offsets per event were estimated to be between

1.2 m and 2.1 m. The moment magnitudes based on total displacements estimated to be in the range of 6.7 to 7.2 Mw. According to dating test results, the oldest occurrence time is estimated to be 27,444 cal BP and assuming the youngest event to have occurred 3 ka ago (based on estimated age of EvI at both scenarios), the average recurrence time is estimated to be  $7,119 \pm 1017$  years. Considering the EvI at both scenarios, the minimum elapsed time is 3 ka and if it is assumed that the last event occurred before  $10,995 \pm 50$  Cal Bp, EvII at scenario A, the maximum elapsed time is therefore  $10,995 \pm 50$  years.

## References

- Allen, M., Ghassemi, M.B., Shahrabi, M.R. & Qorashi, M., 2003. Accommodation of late Cenozoic oblique shortening in the Alborz range, northern Iran, *J. Struct. Geol.*, 25, 659–672.
- Ambraseys, N.N and Melville, C.P., 1982. A history of Persian earthquakes. Cambridge University Press, London, p 219.
- Antoine, P., Bahain, J.J., Berillon, G., Asgari Khaneghah, A., 2006. Tuf calcaire et sequence alluviale en context tectonique actif: La formation de Baliran (province du Mazandaran, Iran). *Quaternaire*, 17, (4), 2006, p. 321-331.
- Asadi, V., 2013. Detection of the Astara Active Fault Using Geomagnetic and Geoelectric Methods. Master's Thesis Geomagnetic and Geoelectric Methods.
- Barzegari, A., Ghorashi, M., Nazari, H., Fontugne, M., Shokri, M.A. and Pourkermani, M., 2017. Paleoseismological analysis along the Astara Fault system (Talesh Mountain, north Iran). *Acta Geologica Sinica-English Edition*, 91(5), pp.1553-1572.
- Berberian, M., 1983. The southern Caspian: a compression depression floored by a trapped modified oceanic crust. *Canadian Journal of earth sciences* 20, 163-183.

- Berberian, M. & Yeats, R.S., 1999. Patterns of historical earthquake rupture in the Iranian Plateau, *Bull. Seismological Society of America.*, 89, 120–139.
- Berberian, M. & Yeats, R.S., 2001. Contribution of archeological data to studies of earthquake history in the Iranian Plateau, *Journal of Structural and Geology.*, 23, 563–584.
- Bronk Ramsey, C., Lee, S., 2013. Recent and planned developments of the program OxCal. *Radiocarbon* 55 (2-3), 720-730.
- Brunet, M.F., Korotaev, M.V., Ershov, A.V. & Nikishin, A.M., 2003. The South Caspian Basin: a review of its evolution from subsidence modeling, *Sedimentary Geology.*, 156, 119–148.
- Davies, R.G., Jones, C.R., Hamzepour, B. & Clark, G.C., 1972. *Geology of the Masuleh Sheet (1:100,000), Northwest Iran*, Technical Report, Geological Survey of Iran, 110 pp.
- Délibrias, G., 1985. Le carbone 14. In: Roth, E., Poty, B. (Eds.), *Methodes de datation par les phénomènes nucléaires naturels: applications*. Masson, Paris, collection CEA pp. 421-458.
- 12- Djamour, Y., P, Vernant., R, Bayer., H.R, Nankali., J.F, Ritz., J.V., Y, Hatam., B, Luck., N, Moigne., M, Sedighi., F, Khorrami., 2010. GPS and gravity constraints on continental deformation in the Alborz Mountain range, Iran, *Geophys Journal International.*, 183, 1287-1301.

- Foroutan, M. S'ebrier, M. Nazari, H. Meyer, B. Fattahi, M. Rashidi, A. Le Dortz, K. and Bateman, M. D., 2012. New evidence for large earthquakes on the Central Iran plateau: palaeoseismology of the Anar fault. *Geophys Journal International*. doi: 10.1111/j.1365-246X.2012.05365. x.
- Jackson, J., Priestley, K., Allen, M., Berberian, M., 2002. Active tectonics of the South Caspian Basin *Geophys Journal International*. 148, 214-245.
- Hessami, K. Jamali, F. Tabassi, H., 2003. Major active faults of Iran, Seismotectonic department, Seismology Research Center.
- Kaz'min, V.G. & Verzhbitskii, E.V., 2011. Age and origin of the South Caspian Basin, *Earth Environmental Sci.*, 51, 131-140.
- Kaveh, A., Nazari, H., Ghorashi, M., Einali, A., Hallaj Neyshabouri, M., 2013. Morphotectonic Map of the Talesh Mountains. Geological Survey of Iran.
- Leroy, S. A. G., A. A. Kakroodi, S. B. Kroonenberg, H. A. K. Lahijani, H. Alimohammadian & A. Nigarov, 2013, Holocene vegetation history and sea level changes in the SE corner of the Caspian Sea: relevance to SW Asia climate. *Quaternary Science Reviews*, 70: 28-47.
- Mangino, S. & Priestley, K., 1998. The crustal structure of the southern Caspian region, *Geophys Journal International*., 133(3), 630-648.
- McCalpin, J.P., 2009. Paleoseismology, Academic Press is an imprint of Elsevier Academic, London, chapter. 1, 2a and 9.

- Mohammadi Vije, M.,2013. Geophysical Study by using of GPR Method for Detection of Active Faults and Sedimentological Investigations in Gillan province. Department of Mining Exploration Aerial Exploration Management, geophysics Group (Geological Survey of Iran).
- Khodabandeh, A.A. Soltani, Gh.A. Babakhani, A.R.,1997. Geological maps of Astara 1:100000 Geological Survey of Iran, Tehran.
- Nazari, H. Ritz, J.-F.Salamati,R. Shafei,A. Ghassemi,A. Michelot, J.-L. Massault, M. and Ghorashi, M.,2009. Morphological and palaeoseismological analysis along the Taleghan fault (Central Alborz, Iran). *Geophys Journal International*. 178, 1028–1041.
- Nazari,H. Ritz, J.-F. Ghassemi, A. Bahar-Firouzi, . K . Salamati, R. Shafei, A.and Fonoudi, M.,2011. Paleoearthquakes Determination of Magnitude~6.5 on the North Tehran Fault, Iran. *Journal of Seismology and Earthquake Engineering*. Vol. 13, No. 1, 2011.
- Nazari,H. Shahidi,A.,2011.Seismotectonic of Iran (Alborz). Geological Survey of Iran, Tehran.97p.
- Rahimzadeh.F.Babakhani,A.R.Eftekhar Nejad.J. Manouchehri,M.,1987. Geological map of Ardbil,Geological Survey of Iran, Tehran. Naqsheh Offset Press, Tehran, Iran.
- Ollivier, V., Fontugne, M., Lyonnet, B., 2015. Geomorphic response and <sup>14</sup>C chronology of base- level changes induced by late quaternary Caspian Sea mobility

(middle Kura Valley, Azerbaijan). *Geomorphology* 230, 109-124.

Reimer, P.J., Bard, E., Bayliss, A., Beck, J.W., Blackwell, P.G., Bronk Ramsey, C., Grootes, P.M., Guilderson, T.P., Haflidason, H., Hajdas, I., Hatté C, C., Heaton, T.J., Hoffmann, D.L., Hogg, A.G., Hughen, K.A., Kaiser, K.F., Kromer, B., Manning, S.W., Niu, M., Reimer, R.W., Richards, D.A., Scott, E.M., Southon, J.R., Staff, R.A., Turney, C.S.M., van der Plicht, J., 2013. IntCal13 and Marine13 radiocarbon age calibration curves 0-50,000 Years cal BP. *Radiocarbon* 55 (4), 1869-1887.

Ritz, J.-F. Nazari, H. Balescu, S. Lamothe, M. Salamati, R. Ghassemi, A. Shafei, A. Ghorashi, M. and Saidi, A., 2012. Paleoearthquakes of the past 30,000 years along the North Tehran Fault (Iran). *Journal of geophysical research*, vol. 117, doi : 10.1029/2012JB009147.

Vernant, Ph., Nilforoushan, b, F., Che ´rya, J., Bayer, R., Djamour, Y., Massona, F., Nankali, H., Ritz, J.-F., Sedighi, M, Tavakoli, F., 2004. Deciphering oblique shortening of central Alborz in Iran using geodetic data. *Earth and Planetary Science Letters* 223 (2004) 177– 185.

Walker, R., 2005. "Quaternary dating methods, 1st edition, Department of Archaeology and Anthropology University of Wales, Lampeter, UK, 286 p.

Wells, D. L., Coppersmith, K. J., 1994. New empirical relationships among magnitude, rupture length,

rupture width, rupture area, and surface displacement. Bull. Seismological Society of America. 84, 974-1002.

Yousefi, E., Friedberg, J.L., 1978. Aeromagnetic map of Iran (Quadrangle No. P4), Geological Survey of Iran. Scale: 1:250000.

Zanjani, A.Z. Ghods, A. Sobouti, F.  
Bergman, E. Mortezaejad, G. Priestley, K.  
Madanipour, S. and Rezaeian, M., 2013. Seismicity in the western coast of the South Caspian Basin and the Talesh Mountains. Geophys Journal International. doi: 10.1093/gji/ggt299.

[http://www.viewfinderpanoramas.org/Coverage%20map%20viewfinderpanoramas\\_org3.htm](http://www.viewfinderpanoramas.org/Coverage%20map%20viewfinderpanoramas_org3.htm).

36-

[http://dds.cr.usgs.gov/srtm/version2\\_1/SRTM30//srtm30](http://dds.cr.usgs.gov/srtm/version2_1/SRTM30//srtm30)